

Organic species in Infrared Dark Clouds¹

T. Vasyunina*, A. I. Vasyunin, Eric Herbst**

Department of Chemistry, University of Virginia, Charlottesville, VA 22904 USA

Hendrik Linz

Max Planck Institute for Astronomy (MPIA), Königstuhl 17, D-69117 Heidelberg,
Germany

linz@mpia.de

Maxim Voronkov

Australia Telescope National Facility, CSIRO Astronomy and Space Science, PO Box 76,
Epping, NSW 1710, Australia

maxim.voronkov@csiro.au

Tui Britton

Department of Physics and Astronomy, Macquarie University, NSW 2109, Australia

Tui.Britton@csiro.au

Igor Zinchenko

Institute of Applied Physics of the Russian Academy of Sciences, Ulyanova 46, 603950
Nizhny Novgorod, Russia

zin@appl.sci-nnov.ru

Frederic Schuller

European Southern Observatory, Alonso de Cordova 3107, Casilla 19001, Santiago 19, Chile

fschull@eso.org

Received _____; accepted _____

*Current address: Max Planck Institute for Radioastronomy (MPIfR), Auf dem Hügel
69, D-53121 Bonn, Germany

** Also: Departments of Astronomy and Physics, University of Virginia, Charlottesville,
VA 22904 USA

ABSTRACT

It is currently assumed that infrared dark clouds (IRDCs) represent the earliest evolutionary stages of high-mass stars ($> 8 M_{\odot}$). Submillimeter and millimeter-wave studies performed over the past 15 years show that IRDCs possess a broad variety of properties, and hence a wide range of problems and questions that can be tackled. In this paper, we report an investigation of the molecular composition and chemical processes in two groups of IRDCs. Using the Mopra, APEX, and IRAM radio telescopes over the last four years, we have collected molecular line data for CO, H₂CO, HNC, CH₃CCH, CH₃OH, CH₃CHO, CH₃OCHO, and CH₃OCH₃. For all of these species we estimated molecular abundances. We then undertook chemical modeling studies, concentrating on the source IRDC028.34+0.06, and compared observed and modeled abundances. This comparison showed that to reproduce observed abundances of complex organic molecules (COMs), a 0-D gas-grain model with constant physical conditions is not sufficient. We achieved greater success with the use of a warm-up model, in which warm-up from 10 K to 30 K occurs following a cold phase.

Subject headings: ISM: clouds, ISM: molecules, Radio lines: ISM, Stars: Formation

1. Introduction

Infrared dark clouds (IRDCs) were first identified by the *Infrared Space Observatory* (*ISO*; Perault et al. 1996) and the *Midcourse Space Experiment* (*MSX*; Egan et al. 1998). Follow-up studies at millimeter, submillimeter, and infrared wavelengths showed that these objects are cold, dense, and have masses from hundreds to thousands of solar masses (e.g., Carey et al. 2000; Rathborne et al. 2006; Peretto & Fuller 2009; Vasyunina et al. 2009; Butler & Tan 2009; Ragan et al. 2011, 2012). Thus, some IRDCs have the potential to harbor not only clusters of low- and intermediate mass stars but also high-mass stars with $M > 8M_{\odot}$ (Kauffmann & Pillai 2010).

Many aspects of IRDCs have now been discussed in the literature. Matters of special attention include the chemical composition and chemical processes in these clouds. The first molecular line study of IRDCs had raised a question concerning the difference between the chemical composition of low-mass pre-stellar cores and IRDCs (Carey et al. 1998). In that survey H_2CO was detected in 10 clouds, thus confirming the presence of dense gas. Using LVG modeling, Carey et al. (1998) estimated the fractional H_2CO abundance to be about 10^{-10} . This is a factor of 50 lower in comparison with low-mass prestellar cores (Ohishi

¹Based on observations carried out with the IRAM 30m Telescope. IRAM is supported by INSU/CNRS (France), MPG (Germany) and IGN (Spain). This publication is based on data acquired with the Atacama Pathfinder Experiment (APEX). APEX is a collaboration between the Max-Planck-Institut für Radioastronomie, the European Southern Observatory, and the Onsala Space Observatory. The 22-m Mopra antenna is part of the Australia Telescope, which is funded by the Commonwealth of Australia for operations as a National Facility managed by CSIRO. The University of New South Wales Digital Filter Bank used for the observations with the Mopra Telescope was provided with support from the Australian Research Council.

et al. 1992). The results of this study tentatively indicate a different chemistry in high- and low-mass star forming regions. However, to distinguish differences and similarities of the chemical composition, we require observational data for more than one molecular species.

Multi-line surveys towards IRDCs have started to appear recently (e.g. Sakai et al. 2008, 2010; Vasyunina et al. 2011; Sanhueza et al. 2012; Hoq et al. 2013). Sakai et al. (2008) observed the $\text{N}_2\text{H}^+(1-0)$, $\text{HC}_3\text{N}(5-4)$, $\text{CCS}(4_3-3_2)$, $\text{NH}_3(1,1)$, (2,2), (3,3), and $\text{CH}_3\text{OH}(7-6)$ lines toward massive clumps associated with IRDCs in order to determine their evolutionary status and to study the chemical conditions within them. Analyzing the $\text{CCS}/\text{N}_2\text{H}^+$ abundance ratio, which is expected to decrease with time, they concluded that infrared dark clouds are chemically more evolved than low-mass pre-stellar cores. In a comprehensive molecular line study, Vasyunina et al. (2011) performed observations toward 15 IRDCs in the frequency range between 86 and 93 GHz using the Australian 22-m Mopra radio telescope. In total, the 13 molecular species N_2H^+ , ^{13}CS , CH_3CN , HC_3N , HNC , HCO^+ , HCN , HNCO , C_2H , SiO , H^{13}CO^+ , H^{13}CN , and CH_3CCH were searched for in all targets. Where possible, Vasyunina et al. (2011) determined molecular abundances and made a comparison with previously obtained abundances for low-mass pre-stellar cores and high-mass protostellar objects (HMPOs).

HMPOs, in comparison with IRDCs, represent a more evolved stage of high-mass star formation (Beuther et al. 2007) where the central protostar has been already formed, but continues accreting material. HMPOs have higher temperatures and appear in emission at mid- and far-IR wavelengths (Sridharan et al. 2002; Beuther & Sridharan 2007). In their molecular line study, Vasyunina et al. (2011) discovered a tendency for IRDCs to have molecular abundances similar to low-mass pre-stellar cores rather than to HMPO abundances on the linear spatial scales probed by the single-dish observations. The study also showed that a direct comparison between observed abundances depends on many

factors and uncertainties. Even if data are obtained with the same instrument, and molecular abundances obtained using similar assumptions, the results would not guarantee the emergence of a clear trend among different source types. As a consequence, to seriously compare the chemistry in HMPOs, low-mass pre-stellar cores, and IRDCs, it is necessary to employ chemical modeling.

Molecular line information collected during the last decade aided the construction of the first, simple, IRDC chemical models (Gibson et al. 2009; Sakai et al. 2012). Still, the results of these models could only be compared with the abundances of a few observed molecules. Vasyunina et al. (2012) presented the first chemical model for IRDCs that uses at least 7 species to constrain the modeling abundances. For that study, a simple 0-D model with a gas-grain reaction network and constant homogeneous physical conditions was used. The modeling was performed for two IRDCs: IRDC013.90-1, which has a lower ammonia kinetic temperature of 13 K, and IRDC321.73-1, which possesses a slightly elevated ammonia kinetic temperature of 25 K. This study showed that observed molecular abundances based on single-dish observations can be reproduced even with a model that contains only a simple physical structure. Moreover, we were able to distinguish a special temperature range between 20 and 30 K, where grain surface reactions have a significant impact on the gas-phase chemistry. Clouds that have these slightly elevated temperatures can indeed feature a different chemistry in comparison not only with HMPOs, but also with low-mass pre-stellar cores. The success of the 0-D model in reproducing single-dish observations of 7 species confirms that it is sufficient to use simple physical models for explaining these types of data. It can be insufficient, however, if we add more complex species.

In the current paper, we concentrate on the analysis of molecular line observations towards IRDCs, and in particular on the behavior of organic species at early stages of

high-mass star formation. Organic species with 6 or more atoms are commonly referred to as COMs (complex organic molecules), and we use this acronym. Surveys by Belloche et al. (2008, 2009); Ikeda et al. (2001) and Remijan et al. (2002, 2003) reveal the presence of COMs in hot cores such as SgrB2, Orion KL, and NGC6334f, which are high-mass star forming regions that are much more evolved than IRDCs. Also, COMs were detected by Rathborne et al. (2008, 2011) in hot cores associated with IRDCs, and in the surveys by He et al. (2012) in the vicinity of so-called Green Fuzzies, or Extended Green Objects (EGOs), which are special regions in IRDCs characterized by an excess of extended 4.5 μm emission in *Spitzer* IRAC imaging, due to H_2 shock-excited emission associated with molecular outflows (e.g. Cyganowski et al. 2008; Chambers et al. 2009).

To explore the possibility of detecting COMs and smaller carbon-containing molecules at earlier stages of high-mass star formation, we collected molecular line data for two groups of IRDCs - northern and southern - in the frequency ranges 71-115 GHz, 152-155 GHz and 213-245 GHz with the Mopra, IRAM, and APEX radio telescopes. In this survey, five COMs were detected along with three smaller species. In southern sources, we detected CO (carbon monoxide), HNCO (isocyanic acid), H_2CO (formaldehyde), CH_3CCH (methyl acetylene), and CH_3OH (methanol), while in addition to these five species, the high sensitivity of IRAM receivers allowed us to detect CH_3CHO (acetaldehyde), CH_3OCH_3 (dimethyl ether), and in one case CH_3OCHO (methyl formate) in northern sources. Molecular abundances for CO, H_2CO , HNCO, CH_3CCH and CH_3OH have already been reported for IRDCs in, e.g., Ragan et al. (2006); Sakai et al. (2008) and Miettinen (2012). Estimated abundances of CH_3CHO , CH_3OCHO and CH_3OCH_3 in IRDCs are reported for the first time.

The paper is structured as follows. The source selection and observations with the Mopra, APEX and IRAM telescopes are described in Section 2. The observed transitions and estimation of the molecular abundances are presented in Section 3. In Section 4, we

compare the results of the previous 0-D pseudo time dependent chemical model and a more realistic physical model that includes a warm-up phase with observational values. We discuss the obtained results in Section 5 and present a summary and our conclusions in Section 6.

2. Observations

2.1. Source description

For the present study, two sets of IRDCs were used, as listed in Tables 1 and 2. All sources were classified according to the criteria described in Vasyunina et al. (2011). Sources that show no emission at 8 and 24 μm were classified as “quiescent”, those that appear in emission at both 8 and 24 μm were identified as “active”. The rest of the clouds, where only 24 μm emission appears, were attributed to a “middle” stage. In addition to this classification, as an indicator of star formation activity we mark the presence of SiO emission based on Vasyunina et al. (2011) and Linz et al. (in prep.), for every source.

A set of southern sources, shown in Table 1, was selected from Vasyunina et al. (2011). There we chose 25 points with $> 3\sigma$ line detections of the four main (1-0) 90-GHz lines: N_2H^+ , HNC, HCO^+ , and HCN. For these southern sources we have estimates of H_2 column density from 1.2 mm Simba/SEST data, temperature estimates from ammonia Parkes observations and kinematic distances from N_2H^+ (1-0) Mopra data (Vasyunina et al. 2011). Here we present new observations of these sources performed with the Mopra and APEX telescopes.

A set of northern sources, shown in Table 2, was taken from previous studies and includes classical clouds from the first studies about molecular line observations in IRDCs (e.g. Carey et al. 1998; Pillai et al. 2006; Simon et al. 2006) as well as the recent work

by Ragan et al. (2012). For these objects, H₂ column densities were estimated based on ATLASGAL 870 μm maps (Schuller et al. 2009); the details of the calculation are provided in Section 3.2. Temperature values were taken from the literature. For those objects where two temperatures are available (for instance, the gas temperature as estimated from ammonia observations, and the dust temperature), we report both values. Ammonia kinetic temperatures were taken from Pillai et al. (2006); Wielen et al. (2012), and Sakai et al. (2008), while dust temperatures were taken from Sanhueza et al. (2012). In the current study for northern sources, we present results from the IRAM and APEX observations.

As an example, observed spectra for six objects: “quiescent”, “middle” and “active” IRDCs for both the southern and northern groups of clouds are presented in Figures 1-7.

2.2. Mopra observations

With Mopra, several observational setups were employed in position switching mode. In all cases, we used the MOPS spectrometer, which allowed us to place 16 “zoom” windows along the 8.3 GHz bandpass and reach a resolution of 0.1 km/s, or 30 kHz. Since for the present study we are interested mainly in organic species, we will focus only on the CO, HNCO, CH₃CCH, and CH₃OH molecules observed with Mopra. Four CO isotopologues: ¹²CO, ¹³CO, C¹⁸O, C¹⁷O, and CH₃OH lines were observed on 27 April-2 May 2011 with the central frequencies of 111.6 GHz and 81 GHz, respectively. The HNCO and CH₃CCH data were obtained by adopting a central frequency of 89.27 GHz, and have been already presented in Vasyunina et al. (2011). Parameters for observed lines can be found in Table 3.

At all frequency setups, we spent in total 15 min “on” source and 15 min on the “off” position. Since for the southern sources no molecular line data were available at the time of the observations, for every source, the “off” position was chosen individually, based only on

an analysis of the Spitzer mid-IR images and by choosing a position with no signs of mid-IR (MIR) extinction. The system temperature during the observations was in the range from 200 K to 300 K. The full-width half-maximum of the beam was measured to be $36 \pm 3''$ at 86 GHz and $33 \pm 2''$ at 115 GHz. The measured beam efficiency corresponds to 0.49 at 86 GHz and 0.42 at 115 GHz (Ladd et al. 2005).

Mopra data were originally stored in a special RPFITS format. The original RPFITS data were then transferred to FITS format using the ATNF spectral line analysis package (ASAP). They were then fed into GILDAS/CLASS for further data reduction and analysis.

2.3. APEX observations

Observations with the APEX telescope in position switching mode were conducted on 25-26 September 2011, 15-18 November 2011 and 12-14 September 2012. Transitions of organic species that were observed during these setups for southern and northern sources are presented in Tables 3-4. The total integration time for each point was around 1-2 min. The “off” source positions were chosen individually for every source, based on the analysis of the CO Galactic Ring Survey (GRS) and MIR Spitzer data. We used the APEX-1 receiver of the Swedish Heterodyne Facility Instrument (SHeFI; Vassilev et al. 2008) with frequency settings at 218.75, 243.25, and 214.77 GHz. The backend for all observations was the eXtended bandwidth Fast Fourier Transform Spectrometer (XFFTS) with instantaneous bandwidth of 2.5 GHz and 32768 spectral channels (Klein et al. 2012). This allowed us to cover the intervals 213 - 220.5 GHz, and 241.5 - 243 GHz for the southern objects and 213-220 GHz for the northern objects with 88.5 kHz spectral resolution. These intervals have the potential to detect many species, including CO, SO, DCO⁺, CH₃OH, etc. However, for the current study, only ¹³CO, C¹⁸O, H₂CO and CH₃OH were selected, as shown in Tables 3-4. At the chosen frequencies, the main beam of the telescope varies

between $30''$ at 211 GHz and $26''$ at 242 GHz. The main beam efficiency is equal to 0.75. The system temperature during the observations was about 140-180 K at 213-220.5 GHz and 210-230 K at 241.5-243 GHz .

The APEX data were observed in service mode and were provided to us by the APEX staff in ready-to-use GILDAS/CLASS format. Therefore, all necessary data reduction was accomplished with the CLASS software.

2.4. IRAM observations

IRAM observations were performed on 8-12 June 2011 in the position switching mode. Total times “on” source and “off” source were determined individually for every source, based on the general strengths of more common lines known from previous measurements, and were between 30 and 60 min in total. The “off” source position was selected to be $600''$ away from the “on” position in the right ascension direction. Pointing was updated every hour, giving a pointing accuracy of around $3''$. The typical system temperature during observations was about 200 K.

For these observations, the EMIR receiver with the Fast Fourier Transform Spectrometer (FTS) as a backend was used. During the observing run, the frequency intervals 76 - 79 GHz and 152.5 - 156.5 GHz were covered with a spectral resolution of 195 kHz. These ranges include lines of several complex organic species, as listed in Tables 4 and 5. According to the IRAM official website, at 86 GHz the beam size is $29''$, and the beam efficiency is 0.81, while at 153 GHz, the telescope beam size is $16''$, and the beam efficiency is 0.74.

The data were analyzed using the GILDAS/CLASS software.

3. Data reduction and analysis

3.1. Observed transitions and detection rates

Among the detected molecules, CO is most abundant gas-phase species, which allows us to detect not only the main CO isotopologue, but also ^{13}CO and C^{18}O . In the southern sources, ^{12}CO (1-0), ^{13}CO (1-0), C^{18}O (1-0), and C^{17}O (1-0) were observed with the Mopra telescope, and ^{13}CO (2-1), and C^{18}O (2-1) were observed with APEX. For northern sources, only APEX observations were performed. Since ^{12}CO and ^{13}CO are most likely optically thick and show complicated line shapes, and C^{17}O was detected only in three regions, C^{18}O was used in all cases to estimate the CO column density and relative abundance with respect to H_2 . It is worth noting that C^{18}O has indeed been found to be optically thin in IRDCs (see, e.g., Hernandez et al. 2011). For southern sources, we used C^{18}O (1-0), as obtained with Mopra, while for northern sources we used C^{18}O (2-1), as obtained with APEX. To reconstruct the CO column density from its isotopologue, we adopted $[\text{C}^{16}\text{O}]/[\text{C}^{18}\text{O}]=500$ from Helmich & van Dishoeck (1997). To derive the CO molecular abundances, we used the H_2 column densities shown in Tables 1 and 2.

HNCO data for our southern clouds were taken from the previous study of Vasyunina et al. (2011), where the detection of HNCO ($4_{0,4}-3_{0,3}$) was reported at 87.925 GHz. The detection rate was 40% among all of the observed clouds. For the northern objects, HNCO ($7_{0,7}-6_{0,6}$) was observed with IRAM at 153.865 GHz. Despite the higher upper state energy related to this transition, HNCO shows a higher detection rate than in the southern sample. In 16 objects out of 18, the detection was stronger than 3σ . Such a high detection rate can be explained by much higher sensitivity of the EMIR receivers at the IRAM 30m telescope.

As shown in Tables 3-4, three transitions of H_2CO were observed in southern and

northern clouds around 218 GHz with APEX. All three transitions were detected only in five southern and four northern objects. For the rest of the targets, only the $(3_{0,3} - 2_{0,2})$ transition was detected. However, even in the sources with all three detections, it was not possible to use the results of the excitation analysis because the lower energy levels were too close for $(3_{2,2} - 2_{2,1})$ and $(3_{2,1} - 2_{2,0})$ transitions. Therefore, for all clouds we used H_2CO $(3_{0,3} - 2_{0,2})$ to determine molecular column densities and abundances.

CH_3OH showed a high detection rate in the southern clouds; however more than three transitions were detected only in six objects, for which we performed excitation analyses. Among these six sources the shape of the excitation diagram allowed us to estimate the methanol column densities and abundances only in three cases: IRDC316.76-2, IRDC317.72-2, and IRDC321.73-1. The other three sources showed a large spread of the points on the population diagram, which might indicate non-LTE behavior. For these sources additional observations are required to build an excitation diagram and extract more realistic excitation temperatures and molecular column densities. In the northern objects, CH_3OH was detected in six clouds out of 18; for two of which, IRDC019.30-1 and IRDC028.34-6, we have enough transitions detected to build a population diagram and estimate an excitation temperature. For the sources with fewer than three detections, molecular abundances were calculated based on CH_3OH $5_{-1,5} - 4_{-1,4}$ E for the southern sources and CH_3OH $4_{2,2} - 3_{1,2}$ E for the northern sources using Equation 1 from Section 3.2. Figure 8 shows CH_3OH excitation diagrams for northern and southern clouds. Estimated column densities are presented in Tables 6 - 7.

For the southern sources, CH_3CCH $J=5-4$ (methyl acetylene) was detected during previous studies in five out of 37 sources (Vasyunina et al. 2011). For two sources, with $K=0, 1,$ and 2 lines, a transition excitation analysis was performed. For the rest, only $K=0$ and 1 transitions had intensities higher than 3σ . Therefore, column densities were

estimated using equation (1) from Vasyunina et al. (2011).

In the northern sources, we observed CH_3CCH $J=9-8$. Eight sources show the presence of $K=0, 1, 2, 3$ components. For these sources, we performed the excitation analysis and estimated CH_3CCH column densities and excitation temperatures. Excitation diagrams for these eight sources are presented in Figure 9. Eight more sources show the presence of only $K=0$ and $K=1$ transitions. For these cases, only the $K=0$ transition and the simple formula from Vasyunina et al. (2011) were used to estimate column densities and abundances.

In the present study, CH_3CHO (acetaldehyde) was covered only in northern targets. The $4_{04}-3_{03}$ $A++$ transition was detected in more than 50% of the clouds, including those that can be qualified as quiescent. The $4_{04}-3_{03}$ E transition, despite a similar upper energy level, was detected only in the six most active regions. This can indicate non-LTE behavior since the two upper states are not degenerate and are of different symmetries. A unique behavior was noticed for IRDC028.34-6, where we detected seven more transitions of CH_3CHO around 77 GHz and 153 GHz and were able to perform an excitation analysis, as shown in Figure 10. See Table 5 and Section 3.5 for more detail.

Our IRAM setup included several transitions of CH_3OCH_3 (dimethyl ether) around 153055 MHz. In five northern objects, we observed quite strong detections. Since these transitions are blended, we used a method described in Requena-Torres et al. (2006) to get a rough estimate of the CH_3OCH_3 abundance. The obtained values can be found in Table 7. The derived abundances of CH_3OCH_3 are listed as upper limits because of the possibility of line-blending with other species.

In the present study, CH_3OCHO (methyl formate) was detected only in the active region IRDC028.34-6, where three transitions were observed, as shown in Table 5. These transitions allowed us to perform an excitation analysis and to estimate the molecular column density and excitation temperature (see Figure 10).

3.2. Molecular Abundance Calculations

Molecular column densities and molecular abundances have been estimated for all observed species. We are assuming that the emission from the COMs is extended and uniformly distributed within the beam of the single-dish observations. Therefore, the beam filling factor is ~ 1 . To estimate column densities we used two methods. For both cases, we assumed LTE conditions and optically thin emission. In the case where only one transition was detected for a particular species (e.g. HNC, H₂CO), we used the following formula to estimate molecular column densities:

$$N_{\text{tot}} = \frac{8\pi}{\lambda^3 A} \frac{1}{J_\nu(T_{\text{ex}}) - J_\nu(T_{\text{bg}})} \frac{1}{1 - \exp(-h\nu/kT_{\text{ex}})} \times \quad (1)$$

$$\times \frac{Q_{\text{rot}}}{g_u \exp(-E_l/kT_{\text{ex}})} \int T_{\text{mb}} d\nu,$$

where λ is the rest wavelength of the transition, A is the Einstein coefficient, g_u is the upper state degeneracy, $J_\nu(T_{\text{ex}})$ and $J_\nu(T_{\text{bg}})$ are values of the Planck function at excitation and background temperatures, respectively, Q_{rot} is the partition function, and E_l is the energy of the lower level (Lee et al. 2009). For g_u , A and E_l , we used values from The Cologne Database for Molecular Spectroscopy (CDMS) (Müller et al. 2001, 2005) for most of the species. For CH₃CHO and CH₃OCHO, values from the JPL database (Pickett et al. 1998) were employed. For the excitation temperatures T_{ex} , we assumed ammonia kinetic temperatures and/or dust temperature from Tables 1 and 2. We calculated the partition function Q_{rot} for every source by interpolating data from the CDMS for the particular source temperature T_{ex} . Integrated intensities $\int T_{\text{mb}} d\nu$ for every species were estimated as areas under the fitted Gaussians (see Tables 8 and 9).

If at least three transitions were detected (e.g. for CH₃OH, and CH₃CCH), an excitation analysis was used to estimate the molecular column density and excitation temperature. Since we assumed that all levels are in LTE, the total column density is

related to the single excitation temperature via the equation

$$\ln \left(\frac{N_u}{g_u} \right) = \ln \left(\frac{N_{\text{tot}}}{Q(T_{ex})} \right) - \frac{E_u}{kT_{ex}}, \quad (2)$$

where N_u , g_u , and E_u are the column density, degeneracy, and upper state energy for the transition. N_{tot} is the total column density, $Q(T_{ex})$ is the partition function at a given temperature, and T_{ex} is the excitation temperature. As in the first case, all necessary parameters were taken from the CDMS and JPL databases. The population diagram for each molecule with at least three detected transitions was formed by plotting $\ln(N_u/g_u)$ against the upper state energy, E_u/k , in Kelvin. When the populations of all levels are in LTE, it should be possible to fit a single straight line to the plotted points. In this case, the slope of the line will be proportional to $1/T_{ex}$. Then the determined excitation temperature can be used for calculating a total column density. The method is described in more detail in, e.g., Goldsmith & Langer (1999).

The H_2 column densities required to convert molecular column densities into fractional abundances were calculated based on 1.2 millimeter SIMBA/SEST (Swedish-ESO Submillimetre Telescope) continuum data for the southern sample, and 870 μm ATLASGAL (The APEX Telescope Large Area Survey of the Galaxy) continuum data for the northern sample. The continuum maps were convolved to the coarser spatial resolution of the respective line observations before extracting the peak fluxes. Then, the following general equation was used:

$$N_{\text{H}_2} = \frac{F_{\text{peak}} R}{\Omega B_\nu(T) \kappa_\nu m_{\text{H}_2}}. \quad (3)$$

Here the measured source peak flux density is given by F_{peak} , Ω is the beam solid angle in steradians, m_{H_2} is the mass of one hydrogen molecule, R is the gas-to-dust ratio, κ_ν is the

dust opacity per gram of dust, and $B_\nu(T)$ is the Planck function at the dust temperature T . We adopt a gas-to-dust mass ratio of 100, an κ_ν value of $1.0 \text{ cm}^2 \text{ g}^{-1}$ and $1.85 \text{ cm}^2 \text{ g}^{-1}$ for the 1.2 mm and 870 μm data respectively, which are values appropriate for cold dense cores (Ossenkopf & Henning 1994). Obtained H_2 column density values are presented in Tables 1-2. Tables 8 and 9 show all necessary line parameters. The resulting molecular abundances for the southern and northern IRDCs are listed in Tables 6 and 7, respectively.

3.3. Temperatures and their influence on molecular abundances

Temperature determination is important for the calculation of observed abundances as well as for the results of models. For example, temperatures that differ by a factor of 2 will give different results for H_2 and molecular column densities and, as a result, abundances will be uncertain by at least a factor of 2-4. As shown in Vasyunina et al. (2012), temperature variations in the chemical model can also significantly change the abundances of most species.

As was mentioned in Section 2.1, for northern sources we use temperature values from Pillai et al. (2006); Sakai et al. (2008); Wienen et al. (2012); Sanhueza et al. (2012) and Pitann et al. (2013). Two ways to estimate temperatures have been used for these sources. The first provides us with the gas temperature and based on the ratio of NH_3 (1,1) and (2,2) inversion transitions, the second enables IR and sub-millimeter data to estimate the dust temperature. For our sample, ammonia kinetic temperatures are typically lower than dust temperatures, as shown in Table 2. Excitation temperatures that we obtained by performing an excitation analysis for CH_3CCH in eight sources are around 30 K; this value is closer to the dust temperatures than to ammonia gas temperatures. Therefore, for the northern clouds, we estimated an upper and a lower limit for the molecular column densities and abundances, using both higher and lower temperatures. In the case where

there is no information about temperature values in a particular source, we assume 10 K as a temperature lower limit and 30 K as a temperature upper limit. Both abundance values are presented as upper and lower limits in Table 7. For the southern sample, for most of the clouds we only had temperature estimates based on the ammonia data, Alternative estimates based on the CH_3CCH and CH_3OH data are available for a few sources. Similar to the northern IRDCs case, these few objects show elevated temperatures, as presented in Table 6. For those sources, where alternative temperature estimate is available, we estimated upper and lower limits for the molecular abundance values.

The differences between calculated gas and dust temperatures might be partially explained by the different telescope beam sizes that were used to obtain these data. Our ammonia Parkes data and data from Sakai et al. (2008) were obtained with an $\sim 70''$ beam, ammonia observations by Pillai et al. (2006) and Wienen et al. (2012) were performed with an $\sim 40''$ beam, while the $16''$ IRAM beam size for the data reported in the current paper is much smaller. In Pitann et al. (2013), dust temperatures based on Herschel data were obtained with the data smoothed to a beam size of $36''$ and temperatures reported in Rathborne et al. (2010) and Sanhueza et al. (2012) were estimated based on IR and sub-millimeter data with beam sizes from $8''$ to $24''$. However, different temperature measurements may also indicate the presence of both cold and warm regions within IRDCs, which are traced by different species.

3.4. Molecular abundance comparisons among IRDCs, HMPOs, hot cores, and low-mass pre-stellar cores

For all molecular species discussed in the current study, there is an abundance variation within one order of magnitude for the northern and southern samples. Such differences are in agreement with our previous work (Vasyunina et al. 2011) and can be explained by the

slight variations in the physical conditions and/or age of the objects.

The detected CO abundance is $\sim 10^{-4}$ for our southern targets, and, depending on the excitation temperature, $\sim 10^{-5}$ – 10^{-4} for the northern targets. The higher CO values of 10^{-4} are in agreement with the Ragan et al. (2006) results for IRDCs and the Helmich & van Dishoeck (1997) results for HMPOs, whereas lower CO values of 10^{-5} lie closer to the typical estimate for low-mass pre-stellar cores from Ohishi et al. (1992) and Tafalla et al. (2006).

The abundances for HNC and CH_3CCH are slightly higher for our southern than for our northern clouds. Taking into account the lower Mopra sensitivity, such a difference can be explained by a selection effect. With the Mopra telescope, we were able to detect these molecules only in the regions with their highest abundance, whereas the high sensitivity of the IRAM telescope allows us also to detect HNC and CH_3CCH also in regions with lower concentration. In general, the calculated HNC and CH_3CCH abundances are still close to low-mass pre-stellar core, HMPO, and hot core values (Sutton et al. 1995; Zinchenko et al. 2000; Marcelino et al. 2009).

The formaldehyde abundances lie in a range between 10^{-10} and 10^{-9} for both southern and northern IRDCs. These values are in good agreement with previous estimates for IRDCs and HMPOs (Helmich & van Dishoeck 1997; Carey et al. 1998). Previous values for low-mass pre-stellar cores have a larger spread from 10^{-10} in L1517B (Tafalla et al. 2006) to 10^{-8} in L134N and TMC-1CP (Ohishi et al. 1992). As was first shown by Mundy et al. (1987) and later adopted to the case of IRDCs by Carey et al. (1998), high abundances of H_2CO are typical for objects with lower densities of $\sim 10^4 \text{ cm}^{-3}$, whereas regions with higher densities of $> 10^5 \text{ cm}^{-3}$ show lower formaldehyde abundances. This result will be discussed in more detail in Section 5. Such behavior might indicate the presence of regions with greater density in high-mass star forming regions, in comparison with some low-mass

pre-stellar cores.

For CH₃OH, we observe a large spread from 10⁻¹⁰ to 10⁻⁸. Such a broad interval is in agreement with previously estimated values for IRDCs by Leurini et al. (2007); Sakai et al. (2010); Miettinen (2012), and Sanhueza et al. (submitted), and with typical 10⁻¹⁰-10⁻⁹ values for low-mass starless cores (Ohishi et al. 1992; Tafalla et al. 2006). Active regions such as Orion and W3 IRS4 and IRS5 also show a large spread in methanol abundances, but with a tendency to higher values: 10⁻⁹ - 10⁻⁷ (Sutton et al. 1995; Helmich & van Dishoeck 1997). Abundance values of 10⁻⁹ and lower can be easily explained by non-thermal desorption and therefore, might correspond to cold “quiescent” regions (Garrod et al. 2007). The higher CH₃OH values of 10⁻⁸ - 10⁻⁷ require an additional warm-up phase induced by stellar heating or the interaction of outflows, as will be discussed in Section 4.3.

While the detection of CH₃CHO and CH₃OCHO in EGOs associated with IRDCs has already been reported in a recent paper by He et al. (2012), we estimate abundances of these species for IRDCs for the first time. The abundance of CH₃CHO lies in the range from 10⁻⁹ to 10⁻⁸, depending on the assumed excitation temperature, for all IRDCs where it was detected (see Table 7), while the abundance of CH₃OCHO in IRDC028.34-6 is 3.7×10⁻¹⁰ for $T_{ex}=30$ K. In more evolved high-mass star forming regions such as HMPOs and hot cores, typical values for CH₃CHO are in agreement with our result (Garrod et al. 2008, and references therein), and CH₃OCHO abundances are similar to our single result or somewhat higher, in the range 10⁻¹⁰ - 10⁻⁸ (Bottinelli et al. 2004; Belloche et al. 2009). However, abundances of both species for low-mass pre-stellar objects lie in the range from 10⁻¹¹ to 10⁻¹⁰ (Bacmann et al. 2012; Cernicharo et al. 2012), which is lower than in IRDCs and hot cores by a factor of 10–10³.

In summary, these comparisons show that there is an overlap in abundances of carbon-bearing species among IRDCs, low-mass pre-stellar cores, HMPOs, and hot cores.

However, the general trend, especially for CH_3OH , CH_3CHO and CH_3OCHO , is to have a higher value in those regions where the temperature is higher, as in HMPOs and especially hot cores.

3.5. The case of IRDC028.34-6

IRDC028.34+0.06 is a relatively well studied and highly structured cloud, with much continuum and molecular line data collected over the past 15 years. It was first mentioned in the pioneering H_2CO study by Carey et al. (1998), where basic parameters as distance and molecular abundance were estimated for IRDCs for the first time. In millimeter and sub-millimeter surveys by Carey et al. (2000) and Rathborne et al. (2006), the entire cloud shows the strongest emission in comparison with other objects of their IRDC samples, and has the highest mass ($> 4000 M_{sun}$) and H_2 column density ($> 10^{23} \text{ cm}^{-2}$). First follow-up studies revealed that the sub-mm continuum emission associated with the northern tip of G28.34+0.06 (component P2 in Carey et al. 1998) does not spatially coincide with the bright slightly extended MIR emission of this part of the cloud (see Figure 11). Indeed, the peak of the sub-millimeter emission is about $8''$ away from the border of the aforementioned MIR emission blob. The sub-millimeter peak does not show emission at 8 micron in the Spitzer/GLIMPSE data but, however, is coincident with a faint 24 micron point source in the Spitzer/MIPS data (cf. Ragan et al. 2012). Such a behavior indicates the presence of different evolutionary stages in relatively close vicinity. High resolution Submillimeter Array (SMA) observations performed by Zhang et al. (2009) revealed the presence of CH_3CN emission associated with IRDC028.34-6 and provided an excitation temperature estimate of 120 K. This detection might indicate the presence of a small hot core associated with this sub-millimeter source when observed with arcsecond resolution.

In IRDC028.34-6 we detect more molecular lines than in any other target. All obtained

spectra are presented in Figure 7. Moreover, it is the only source where methyl formate was detected. Additional transitions for COMs and smaller carbon-containing species, detected only in IRDC028.34-6 during the current study within the passband of the IRAM 30m observations at 76 GHz and 153 GHz, are presented in Table 5.

Since two temperature estimates are available in the literature for IRDC028.34-6, a value of ≈ 16 K based on the Pillai et al. (2006) ammonia data and a higher value of 33 K based on the Sanhueza et al. (2012) dust analysis, both values were used to estimate abundances of CO, HNC, and H₂CO, as shown in Table 7. Detection of several transitions for CH₃OH, CH₃CCH, CH₃CHO, and CH₃OCHO allowed us to perform excitation analyses and obtain a more reliable estimate of the excitation temperature and relative abundances, which are presented in Table 7.

In the next section, we will report a comparison between model results and molecular observations for IRDC028.34-6. In order to make a model that is more reliable and to analyze the behavior of organic species and cold and dense gas tracers simultaneously, the molecular abundances of HNC, HCO⁺, N₂H⁺, NH₃, C₂H, and HC₃N were used in addition to the organic molecules presented in the current paper. The additional abundances were taken from previous studies by Pillai et al. (2006) and Sanhueza et al. (2012). All observational abundances used for the comparison with model results are presented in Table 10.

4. Modeling of IRDC028.34-6

4.1. 1-Phase 0-D Model with constant temperature

In Vasyunina et al. (2012), we reproduced abundances of eight cold and dense gas tracers, using a 0-D gas-grain pseudo time-dependent model. As a test of this simple

approach, we have attempted to reproduce abundances of additional organic species with four different sets of conditions. In all cases, the H_2 density is 10^5 cm^{-3} , while the temperatures are 15, 25, 35 and 120 K. These correspond to the ammonia kinetic temperature, the excitation temperatures of acetaldehyde (CH_3CHO), and methyl acetylene (CH_3CCH), the dust temperature, and the CH_3CN excitation temperature obtained by Zhang et al. (2009) respectively. In this study, we adopted the same gas-grain network as in Vasyunin & Herbst (2013a), which includes gas-phase, gas-grain interactions and reactions on the grain surface. This is a version of the KIDA network with an addendum of grain-surface chemical reactions originally published in Semenov et al. (2010).² The granular chemistry was treated by rate equations, rather than the more advanced and computer-intensive stochastic approaches (Vasyunin & Herbst 2013a). Elemental abundances and initial abundances were taken from Wakelam & Herbst (2008) (see also Morton 1974; Graedel et al. 1982) for the low metal case. Other than hydrogen, which starts out totally in molecular form, the initial species are atomic in nature. The grains are initially bare. The cosmic ray ionization rate is assumed to be the canonical value for atomic hydrogen of $1.3 \times 10^{-17} \text{ s}^{-1}$. The observed H_2 column density of $8.3 \times 10^{22} \text{ cm}^{-2}$ corresponds to a visual extinction $A_V \approx 90$ (according to Ryter 1996). Unlike the previous study, together with thermal and cosmic ray desorption, we include photo-desorption processes, with a yield per photon of 10^{-3} for all species, according to suggestions by Öberg et al. (2007). Reactive desorption, as described in Garrod et al. (2007), was not taken into account in Vasyunina et al. (2012) and was not included in the initial calculations for the current study.

Figure 12 shows modeled abundance profiles for times up to 10^6 yr for 14 species. The boxes in the panels represent observational values for IRDC028.34-6 with respect to

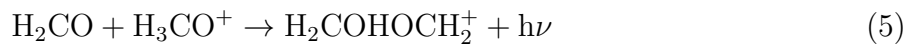
²kida.obs.u-bordeaux1.fr/uploads/models/benchmark_2010.dat

$\text{H}_2 \pm$ one order of magnitude. We reach agreement within an order of magnitude between model and observations for HNC, HCO^+ , CCH, HC_3N , H_2CO , NH_3 , and CO at all four temperatures, and for N_2H^+ at 15 and 25 K, in a time range between 10^4 and 10^5 yr. However, we cannot reproduce the abundances of the five organic species CH_3OH , HNCO, CH_3CCH , CH_3CHO , and CH_3OCHO in the gas phase with either of the four chosen temperatures. Indeed, differences between model and observational abundances can reach more than two orders of magnitude at all times. The chemistry leading to these differences is discussed below.

The primary formation route of methanol is the hydrogenation sequence on surfaces of interstellar grains:



which is proved to be efficient at a temperature of 10 K (Charnley et al. 1997; Watanabe & Kouchi 2002) but not at the higher temperatures considered here (i.e. $T > 15$ K) because the residence time of H atoms on grains becomes too short and reaches just a few minutes. By 10^6 yr at 10 K, the fractional abundance of methanol on grain surface reaches $\sim 10^{-5}$. However, despite being efficiently formed on grain surface at 10 K, methanol has no efficient way to be transferred to the gas phase at this temperature, because the non-thermal desorption processes in the considered model (see above) are all inefficient. The most efficient method to produce methanol in the gas phase is via the slow reaction



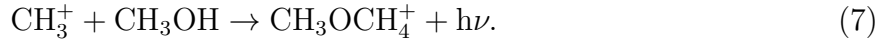
described in Horn et al. (2004), followed by the subsequent dissociative recombination. The rate coefficients of the reactions involving the ion $\text{H}_2\text{COHOCH}_2^+$ are highly uncertain because the products involve a major shift in the positions of the hydrogen atoms. Interestingly, the dissociative recombination of $\text{H}_2\text{COHOCH}_2^+$ has two channels in our

network: methanol, with a probability of 0.99, and methyl formate (CH_3OCHO) with a probability of 0.01. This fact explains the strong similarity of the abundance profiles between methanol and methyl formate in Figure 12. The surface route of formation of methyl formate via the reaction



is inefficient at 10 K due to the negligible mobility of reactant radicals. For models with constant temperature greater than 10 K, the methoxy radical (CH_3O) cannot be produced efficiently because of the difficulty in hydrogenating CO into methanol via eq. (4) at these temperatures. As such, there is no way to produce methyl formate on grain surfaces in models with constant temperature.

Dimethyl ether CH_3OCH_3 is also produced only via a gas-phase route in the absence of efficient non-thermal desorption. After production of its protonated ion $\text{CH}_3\text{OCH}_4^+$, the ether is formed in the subsequent dissociative recombination. The ion is produced via the slow reaction

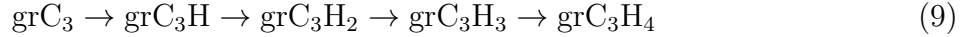


This radiative association is inefficient in the considered isothermal cases, but can be an efficient source of dimethyl ether in hot cores when the gas phase is rich in methanol (e.g., Garrod & Herbst 2006; Vasyunin & Herbst 2013a). The grain surface formation of CH_3OCH_3 via the reaction



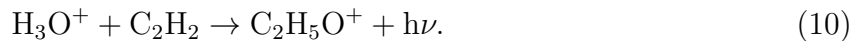
can occur at $T \geq 25$ K. But again, in models with constant temperature above 10 K, this channel will not work for the reason same as discussed above for methyl formate; viz., the absence of surface atomic hydrogen to produce methanol and other hydrogenated species such as CH_3 and CH_3O .

Methyl acetylene (CH_3CCH) has both gas-phase and grain-surface formation routes. In the gas phase, it is formed via a sequence of ion-molecule reactions involving small carbon-chain molecules. On the grain surface, CH_3CCH is produced via the hydrogenation of C_3 via reactions with surface hydrogen atoms:

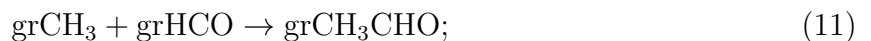


At 10 K, methyl acetylene production occurs via both routes. However, since there is no efficient desorption mechanism at 10 K in the model, CH_3CCH produced on grains remains locked there. At the same time, gas-phase CH_3CCH is quickly accreted onto grains due to the relatively high gas density of 10^5 cm^{-3} . Thus, the resulting fractional abundance of methyl acetylene in the gas is $\sim 3 \times 10^{-11}$. Not surprisingly, at higher temperatures of 25–120 K, the peak abundance of CH_3CCH remains almost unchanged; the grain-surface formation route becomes inefficient due to the same reason as the route of methanol formation, while the ion-molecule gas-phase reactions exhibit only a weak dependence on temperature.

Acetaldehyde (CH_3CHO) in the gas phase is only produced directly via the dissociative recombination of its protonated precursor, which is synthesized in the gas-phase reaction.



The reactants are produced via simple ion-molecular chemistry. The efficiency of this channel is low, and the peak fractional abundance of acetaldehyde only reaches $\sim 10^{-12}$ with respect to hydrogen at all temperatures studied. On the grain surface, CH_3CHO can be formed via the reaction



however, at 10 K this reaction is inefficient because the grCH_3 and grHCO radicals have low mobilities. At temperatures of 25–120 K, the mobility of the reactants is appreciable, but

the abundances of the radicals is low, because they are produced via the photodissociation of methanol and formaldehyde. These species are in turn produced by the hydrogenation of CO, which is itself efficient only at low temperatures near 10 K. Consequently, there is no way to produce acetaldehyde in appreciable amounts in our models with constant temperature.

For gaseous HNCO, the formation route is a grain-surface reaction



This reaction is efficient even at 10 K, and the surface abundance of HNCO in our model reaches a relatively high value of 10^{-6} . Due to the lack of an efficient desorption mechanism for HNCO at $T < 45$ K in our model, the gas-phase abundance of HNCO is low.

These examples illustrate the fact that the constant temperature and density approach works only when we analyze simple molecules, which all trace cold and dense material. In the case where we seek to explain the behavior of more complex species, we need to employ a more complex model with time-dependent physical conditions and additional processes such as non-thermal reactive desorption (Garrod et al. 2007).

4.2. 1-Phase 0-D Model with reactive desorption and constant temperature

To improve our results for complex species in IRDC0028.34-6, we included an additional process, reactive desorption, and, subsequently, a warm-up phase in the model. The reactive desorption is non-thermal desorption from interstellar dust grains via exothermic surface reactions, which was described and applied to the case of low-mass pre-stellar cores by Garrod et al. (2007). There it was shown that reactive desorption plays an especially important role in reproducing the abundances of gaseous organic species such as CH₃OH. However, in many studies this process is not taken into account, because extensive

laboratory evidence for it is lacking. In the current study, we assume that the efficiency of the reactive desorption is 1%; that is, 1% of the products of a chemical reaction on a grain desorb into the gas while 99% remain.

Figure 13 shows the improvement that we obtain after adding reactive desorption to the simple model discussed previously. The cold dense gas tracers and CO are still reproduced well in the time range 10^4 - 10^5 yr at all four temperatures, except N_2H^+ , which exhibits agreement between model and observation only at 15 and 25 K. All COMs and smaller carbon-containing species, except CH_3OCHO , show at least a 1-2 order-of-magnitude increase in abundance at 15 and 25 K, the two lower temperatures studied. The gas-phase abundance of methyl formate remains almost unchanged in comparison with Figure 12 because it is still mostly produced via the dissociative recombination of its protonated form made in reaction (5). The abundances of the reactants of this reaction, formaldehyde and protonated formaldehyde, are governed by gas-phase chemistry, and only slightly affected by the introduction of reactive desorption in the model. The abundances of HNCO , CH_3CHO and CH_3OCH_3 increase also at 35 K.

After we add reactive desorption, the dominant chemical processes of the organic species on the grain surface and in the gas phase become more dependent on the temperature. At 15 and 25 K, CH_3CHO , CH_3OCHO and CH_3OCH_3 still form mainly in the gas phase via reactions discussed in the previous section. Moreover, including reactive desorption increases the abundances of their parent ions, which leads to at least some increase in the abundance of the resulting neutral species (Vasyunin & Herbst 2013b). At the same temperatures, reactive desorption becomes the main formation mechanism for CH_3OH , CH_3CCH and HNCO that are formed in reactions (4), (9) and (12), correspondingly, and then ejected to the gas.

As the temperature increases to 35 K, the gas-phase abundances of all considered

COMs, except CH_3CHO and CH_3OCHO , are significantly enhanced by reactive desorption, which is their dominant formation mechanism. However, at this temperature the abundances of parent radicals such as grCH_3 and grCH_3O are lower than at 10 and 25 K. Hence, although reactive desorption becomes a dominant formation route, it is not efficient enough to produce the required amount of the observed COMs. A further increase in temperature to 120 K entirely kills grain-surface chemistry, which eliminates the effects of reactive desorption. Correspondingly, the abundances of species at 120 K become very similar to those in the model without reactive desorption. Only for HNCO at 10, 25 and 35 K, and CH_3CCH at 10 and 25 K can the observational abundances be explained by including reactive desorption. Modeled abundances for CH_3CHO and CH_3OCHO are still too low at all four temperatures, and CH_3OH is reproduced only at 10 K at the very early time range 10^3 - 10^4 yr with predicted abundances reaching values of $\sim 10^{-10}$. Clearly, further improvement is required to explain the abundances of the COMs and smaller organic species.

4.3. 2-Phase 0-D Model: Cold and Warm-up Phase

We next include a warm-up phase in the model. As stated previously, the phase can be due to stellar heating or the interaction of shock waves in outflows (Arce et al. 2008; Viti et al. 2004). For IRDCs, even ammonia temperatures are elevated to 15-25 K, in comparison with the usual 10 K for low-mass pre-stellar cores. Dust temperatures from Sanhueza et al. (2012) and excitation temperatures obtained from the CH_3CCH analysis are even higher at ~ 30 K. In the first phase of our warm-up model, which lasts for 10^6 yr, the temperature and density remain at 10 K and 10^5 cm^{-3} , respectively. In the second phase, the density stays the same, while the temperature increases from 10 to 30 K over 6.5×10^4 yr with a $T \propto t^2$ time dependence (see Garrod & Herbst 2006), and remains constant after it reaches

a maximum value of 30 K. The cold phase is notable for the production of methanol and formaldehyde on the ice.

Fractional abundances relative to H_2 as a function of time for 14 gas-phase species starting at 10^4 yr into the warm-up phase are presented in Figure 14. The gradual temperature increase after the 10^6 -yr cold phase leads to an enhancement of all molecules discussed in the paper, including CH_3OH , CH_3CHO , and CH_3OCHO . During the cold phase, precursor species such as formaldehyde and methanol collect on the grain surface. As the temperature begins to increase, surface radicals are formed mainly by photodissociation processes and then begin to diffuse and react to form larger amounts of more complex species. (e.g. Garrod et al. 2008). Reactive desorption then results in greater abundances of gas-phase COMs compared with the same process at all four constant temperatures discussed above.

The abundances of 12 species covered by the observations can be reproduced simultaneously by the model described above at 3×10^5 yr, which is somewhat after the final temperature of 30 K is reached. Methanol is an exception; in this case, the agreement occurs before 6×10^4 yr; i.e., when the temperature is still below 20 K. When the temperature exceeds 20 K, CO evaporates from the grain surface. This process leads to an increase in the abundance of HCO^+ , which destroys methanol in the gas. Additionally, at 30 K, the accretion rates of gas-phase molecules including methanol are faster than at 10 K, which also suppress their abundance. In Section 5, we will discuss physical conditions that might better explain the observed CH_3OH values.

5. Discussion

The results of our warm-up model with a prior cold phase show that both phases are required to reproduce COMs in IRDC028.34-6, although there is no single period of time where all of the species are reproduced. In an attempt to improve our model, we have varied some of the parameters. Figure 15 shows the results of six warm-up models with a variety of different parameters, while Table 10 lists a larger number of abundances for these different models and our standard model at a time of 3×10^5 yr into the warm-up phase, when the best fit between model and observations is reached.

To investigate the influence of reactive desorption on our results, we ran the standard chemical model with a higher efficiency of 10%. The results of this model are presented in Figure 15. The more effective reactive desorption significantly increases the abundances of most of the COMs. The increase leads to much better agreement between model and observations for CH_3OCHO at 3×10^5 yr and CH_3OCH_3 at 6×10^4 yr. However, the methanol abundance still decreases after the temperature becomes higher than 20 K and the formaldehyde abundance becomes one order of magnitude too high in the model. Taking into account the overall agreement between model and observations, we can conclude that the higher efficiency for reactive desorption does not provide us with a better fit to the abundances if we consider abundances for all available species and not only COMs such as CH_3OCHO and CH_3OCH_3 .

Since some of the species might also trace denser regions, we ran an alternative chemical model with the higher density of 10^6 cm^{-3} . The upper left panel of Figure 15 shows that the increase in density leads to a reduction of the abundances for most of the species. As a result, the modeled abundances of HNCO , CH_3CHO , CH_3OCHO , N_2H^+ and HNC become more than one order of magnitude different from the observational values. However, in the case of formaldehyde, the abundance drop leads to a better agreement between model and

observations. Such behavior might suggest that we detect species that actually are located in different parts of the cloud. For example, H_2CO might trace more dense regions, while HNCO , CH_3OCHO , N_2H^+ and HNC might dominate in regions with lower density.

In a similar way, the standard model with a shorter cold phase lasting only 10^5 yr leads to a reduction of the gas-phase abundances for the most of the discussed species, as shown in the upper right panel of Figure 15. An extended cold phase of 10^7 yr also results in lower COM abundances. That indicates that the duration of the cold phase plays an important role in the formation of the COMs considered in the present paper.

In addition to the cold phase, we need to look at the results of variations in the parameters for the warm-up phase, such as the shape of the temperature profile, the warm-up time, and the final temperature value. For our standard warm-up model, we used a quadratic temperature profile from Garrod & Herbst (2006). However, unlike their study, we increased the temperature to only 30 K, because this value is consistent with dust temperatures reported in Sanhueza et al. (2012) and excitation temperatures obtained from the excitation analysis of CH_3OH and CH_3CHO . An increase in the final temperature to 40 K results in a drop of 2 orders of magnitude for the gas-phase abundances of HNCO and CH_3OCH_3 , and a behavior very similar to that at 30 K for CH_3CHO and CH_3OCHO , as can be seen in the lower left panel of Figure 15. The only species where we achieve significant improvement at 40 K is CH_3OH . At this higher final temperature, the methanol fractional abundance reaches 3×10^{-8} at 10^5 yr after the warm-up begins. This value is in a good agreement with the value of 4×10^{-8} obtained from observations and shows that methanol can at least partly come from regions with a higher temperature. As can be seen in Figure 15, the further increase of the final temperature to 120 K will lead to more than two orders of overprediction for most of the species including CH_3OH , HNCO , CH_3CCH , CH_3CHO , HCCCN , HNC , and NH_3 . However, beam dilution in a single-dish observation

is also possible. In this case, when a compact hot core is deeply embedded within an IRDC, the estimated observational abundances would be at least two orders of magnitude higher, and hence, show good agreement with a higher final temperature model. The tracers of cold and dense gas, in such a model, might exist in the outer shell with lower temperature. Nevertheless, with a hot core temperature in IRDC028.34-6, we will not be able to reproduce the abundances of most of the observed molecules with the homogeneous warm-up model.

An extensive comparison between observations and modeling results with the shorter duration of the cold phase, higher final temperature and higher density shows that the abundances of some species at 3×10^5 yr, such as CO, CH₃CCH, HCO⁺, C₂H and NH₃, do not depend on these variations in conditions. Species as H₂CO, CH₃OH, CH₃OCH₃ and HNC, on the contrary, are very sensitive to these changes. This conclusion has to be taken into account in future studies on “IRDC-like” environments; i.e., temperatures between 15 and 30 K, and densities in the range of 10^5 - 10^6 cm⁻³.

Apart from the T_{tot}^2 temperature warm-up, we also ran the code with a more rapid and less rapid (linear) warm-up. For the rapid warm-up, we increased the temperature as a step function from 10 to 30 K immediately after the 10^6 yr of the cold phase. This warm-up gives reasonable abundances for most of the species except formaldehyde and methanol, which become significantly under-abundant in the model, even though the methanol abundance on the grain surface after the very rapid warm-up and after the original T_{tot}^2 temperature rise are similar. For the linear warm-up, the maximum temperature was reached at 6×10^4 yr after the start of the warm up. As shown in the lower right panel of Figure 15, the final results of this model lie very close to those of our standard model. Consequently, we are once again able to reproduce the abundances of most of the species at 3×10^5 yr, except for methanol. Hence, at the considered temperature, density and time ranges, the shape

of the temperature profile does not play as significant a role for the selected molecular species as the density value or the duration of the cold phase. Nevertheless, the shape of the temperature profile might help to explain the composition of warmer and more evolved regions, which we do not consider here. To better test the shape of the warm-up profile at the current conditions, we need to include observational abundances for additional species that might be more sensitive to such changes.

6. Summary and Conclusions

In the current paper, we have presented new molecular line observations for a variety of IRDCs. In total, eight COMs and smaller carbon-containing species were detected: CO, HNCO, H₂CO, CH₃CCH, CH₃OH, CH₃CHO, CH₃OCHO and CH₃OCH₃. For all species, molecular column densities and abundances were estimated. The calculated molecular abundances are typically in agreement with previously obtained IRDC values if available. A direct comparison with abundances for low-mass pre-stellar cores, HMPOs, and hot cores reveals that COM abundances in IRDCs tend to be higher than in low-mass pre-stellar cores, although they do not reach the maximum HMPO and hot core values.

To better understand the chemical processes in IRDCs, we built a chemical model with warm-up and including reactive desorption, and compared model and observational results for IRDC028.34-6. Our study shows that one promising way to explain the abundances of organic species in IRDCs is to quadratically increase the temperature from 10 to 30 K after a 10⁶ yr duration of the cold phase. Although the results depend more on the duration of the cold phase than on the temperature profile, too fast a warm-up can cause a drop in the abundance of some organic species when the final temperature is reached. Our model represents the general trend in observed molecular abundances very well. However, it has to be noticed that since some species are very sensitive to changes in the temperature and

density conditions, to get better agreement between the model and observations, it is better to run a separate chemical model for each object with physical parameters different from what was discussed in Sections 4.2 and 4.3.

The temperature increase that occurs in the IRDC environment can be caused by the beginning of the star formation processes in the cloud, or by the influence of outflows and shocks from nearby regions. The results of our study show that the analysis of organic species allows us not only to understand the chemical processes, but also to reconstruct any change in physical conditions, such as warm-up, that may take place in IRDCs.

EH wishes to acknowledge the support of the National Science Foundation for his astrochemistry program, and his program in chemical kinetics through the Center for the Chemistry of the Universe. He also acknowledges support from the NASA Exobiology and Evolutionary Biology program through a subcontract from Rensselaer Polytechnic Institute. IZ was partially supported by the Russian Academy of Sciences, the Ministry of education and science of Russian Federation (project 8421) and Russian Foundation for Basic Research (grant RFBR 12-02-00861).

We would like to thank an anonymous referee for valuable comments and suggestions, which helped to improve the paper significantly. This research has made use of the NASA/IPAC Infrared Science Archive, which is operated by the Jet Propulsion Laboratory, California Institute of Technology, under contract with the National Aeronautics and Space Administration. The 22-m Mopra antenna is part of the Australia Telescope, which is funded by the Commonwealth of Australia for operations as a National Facility managed by CSIRO. The University of New South Wales Digital Filter Bank used for the observations with the Mopra Telescope was provided with support from the Australian Research Council.

Facilities: Nickel, HST (STIS), CXO (ASIS).

Table 1. List of observed southern IRDCs.

Name	R.A. (J2000.0)	Decl. (J2000.0)	Distance ^a (kpc)	T ^a (K)	N(H ₂) ^a ×10 ²² cm ⁻²	category ^c
IRDC309.13-1	13 45 17.521	-62 22 02.84	3.9	16.3	0.6	M
IRDC309.13-2	13 45 22.610	-62 23 27.48	3.9	14.7	0.5	M
IRDC309.13-3	13 45 16.775	-62 25 37.25	3.9	35.4	0.4	A
IRDC309.37-1	13 48 38.532	-62 46 17.55	3.4	31.4	0.9	A
IRDC309.37-2	13 47 56.116	-62 48 33.46	3.4	15.7	0.8	A
IRDC309.37-3	13 48 39.383	-62 47 22.39	3.4	15.7	0.7	Q
IRDC309.94-1	13 50 54.970	-61 44 21.00	5.3 ^b	48.8	5.2	A
IRDC310.39-1	13 56 01.359	-62 14 18.29	4.2	27.4	1.2	A, SiO
IRDC310.39-2	13 56 00.759	-62 13 59.80	4.2	27.4	1.2	A
IRDC313.72-1	14 22 53.158	-61 14 41.00	3.3	19.9	0.4	A, SiO
IRDC313.72-2	14 22 57.151	-61 14 10.84	3.3	19.9	0.4	A, SiO
IRDC313.72-3	14 23 02.720	-61 13 39.64	3.3	19.9	0.3	Q, SiO
IRDC313.72-4	14 23 04.533	-61 14 46.00	3.3	19.9	0.4	Q, SiO
IRDC316.72-1	14 44 19.000	-59 44 29.00	2.7	26.1	1.2	M
IRDC316.72-2	14 44 15.400	-59 43 20.00	2.7	24.3	1.3	Q
IRDC316.76-1	14 44 56.000	-59 48 08.00	2.7	22.6	4.1	A, SiO
IRDC316.76-2	14 45 00.500	-59 48 44.00	2.8	23.2	4.8	A
IRDC317.71-1	14 51 06.905	-59 16 11.03	3.0	15.6	1.2	Q
IRDC317.71-2	14 51 10.975	-59 17 01.73	3.0	16.6	3.5	A
IRDC317.71-3	14 51 19.667	-59 17 43.77	3.2	15.6	0.6	Q, SiO
IRDC321.73-1	15 18 26.387	-57 22 00.14	2.2	22.0	1.0	M, SiO
IRDC321.73-2	15 18 01.693	-57 22 02.00	2.2	11.7	1.7	M
IRDC321.73-3	15 18 01.065	-57 21 24.48	2.1	11.7	1.7	A
IRDC013.90-1	18 17 33.378	-17 06 36.70	2.5	12.9	2.6	M
IRDC013.90-2	18 17 19.350	-17 09 23.69	2.4	13.4	1.1	Q

^adistance, kinetic temperature, and H₂ column density are taken from Vasyunina et al. (2011)

^bfrom Saito et al. (2001)

^cMIR classification: "A" indicates "active" cores, "M" - "middle", "Q" - "quiescent", "SiO" - detected SiO emission as described in Vasyunina et al. (2011) and Linz et al. (in prep.) (see text in Section 2.1).

Table 2: List of observed northern IRDCs.

Name	R.A. (J2000.0)	Dec. (J2000.0)	Distance (kpc)	T_{kin} [T_{dust}] (K) [(K)]	$N(H_2)$ $\times 10^{22} \text{ cm}^{-2}$	Category	Ref.
IRDC010.70-2	18:09:45.6	-19:42:07.9	3.46	15	2.5	A,SiO	1
IRDC010.70-4	18:09:58.1	-19:48:43.4	3.46	16	1.8	A,SiO	1
IRDC011.11-2	18:10:33.5	-19:21:47.0	3.6	14	2.3	Q,SiO	2,3
IRDC011.11-4	18:10:28.3	-19:22:31.5	3.6	13	4.2	A,SiO	2,3
IRDC011.11-5	18:10:18.1	-19:24:37.8	3.6		3.1	Q	2,3
IRDC013.90-1	18:17:34.9	-17:06:48.1	2.5	13	3.5	Q/M	4
IRDC015.05-2	18:17:38.8	-15:48:47.3	3.2	[30]	1.8	Q,SiO	5,6
IRDC015.05-3	18:17:50.4	-15:53:37.4	3.2	15 [23]	1.5	Q	5,6
IRDC018.48-7	18:25:22.89	-12:54:50.7	3.5		2.3	M	7,8
IRDC018.48-8	18:25:14.46	-12:54:08.8	3.5		1.1	Q,SiO	7,8
IRDC019.30-1	18:25:58.5	-12:03:59	2.2	15	2.0	A,SiO	2,3,6,9
IRDC028.34-3	18:42:50.9	-04:03:14	4.8	16 [32]	2.2	M,SiO	2,3,6
IRDC028.34-4	18:42:46.6	-04:04:11.5	4.8	13 [24]	2.5	M,SiO?	2,3,6
IRDC028.34-6	18:42:52	-03:59:54	4.8	16 [33]	8.3	A,SiO	2,3,6
IRDC048.66-1	19:21:49.9	13:49:34.7	2.5	[19]	1.6	A,SiO	5,10
IRDC048.66-3	19:21:44.7	13:49:25.7	2.5	[17]	1.5	Q,SiO	5,10
IRDC079.31-2	20:31:57.5	+40:18:30	1/2.36	13	14.2 ^a	Q	2,3
ISOSSJ23053	23:05:21.7	+59:53:43	4.31	14[17]	4.5 ^b	M	9,11,12

Notes: Kinetic temperature estimated based on ammonia measurement and dust temperature; H_2 column density calculated adopting 29'' beam size and ammonia kinetic temperature; category is determined according to MIR classification (see Table 1).

(a) H_2 column density adopted from Pillai et al. (2006), (b) H_2 column density calculated based on SCUBA 850 μm flux estimate from Birkmann et al. (2007).

(1) Wienen et al. (2012), (2) Pillai et al. (2006), (3) Carey et al. (1998), (4) Vasyunina et al. (2011), (5) Rathborne et al. (2006), (6) Sanhueza et al. (2012), (7) Sakai et al. (2008), (8) Sridharan et al. (2002), (9) Ragan et al. (2012), (10) Pitann et al. (2013), (11) Birkmann et al. (2007), (12) Wouterloot et al. (1988).

Table 3: Transitions of organic species observed for southern IRDCs.

Molecule	Transition	Rest frequency (MHz)	A ($\times 10^{-5} \text{ s}^{-1}$)	g_u	E_{up}/k (K)	Telescope	Beam ($''$)
CH ₃ OH	5 _{-1,5} -4 _{0,4} E	84521.206	0.196	11	40.39	Mopra	36
CH ₃ CCH	5 ₂ -4 ₂	85450.7	0.170	22	41.21	Mopra	36
CH ₃ CCH	5 ₁ -4 ₁	85455.6	0.194	22	19.53	Mopra	36
CH ₃ CCH	5 ₀ -4 ₀	85457.2	0.202	22	12.30	Mopra	36
HNCO	4 ₀₄ -3 ₀₃	87925.238	0.878	9	10.54	Mopra	36
C ¹⁸ O	1-0	109782.176	0.0062	3	5.26	Mopra	33
¹³ CO	1-0	110201.354	0.0063	6	5.28	Mopra	33
C ¹⁷ O	1-0 F=3/2-5/2	112358.780	0.0066	4	5.39	Mopra	33
C ¹⁷ O	1-0 F=7/2-5/2	112358.988	0.0066	8	5.39	Mopra	33
C ¹⁷ O	1-0 F=5/2-5/2	112360.005	0.0066	6	5.39	Mopra	33
CO	1-0	115271.201	0.0072	3	5.53	Mopra	33
CH ₃ OH	1 _{1,0} - 0 _{0,0} E	213427.1	3.370	3	23.36	APEX	~30
H ₂ CO	3 _{0,3} - 2 _{0,2}	218222.2	28.177	7	20.95	APEX	~29
H ₂ CO	3 _{2,2} - 2 _{2,1}	218475.6	15.714	7	68.09	APEX	~29
H ₂ CO	3 _{2,1} - 2 _{2,0}	218760.0	15.776	7	68.11	APEX	~29
CH ₃ OH	4 _{2,2} - 3 _{1,2} E	218440.0	4.687	9	45.45	APEX	~29
C ¹⁸ O	2-1	219560.3	0.0601	5	15.80	APEX	~29
¹³ CO	2-1	220398.6	0.0607	10	15.86	APEX	~29
CH ₃ OH	5 _{0,5} - 4 _{0,4} E	241700.1	6.0367	11	47.93	APEX	~26
CH ₃ OH	5 _{-1,5} - 4 _{-1,4} E	241767.2	5.8049	11	40.39	APEX	~26
CH ₃ OH	5 _{0,5} - 4 _{0,4} A+	241791.3	6.0478	11	34.81	APEX	~26

Notes: Einstein A coefficients, degeneracy, and lower state energy levels for all molecules taken from CDMS Catalog (<http://www.astro.uni-koeln.de/cdms/catalog>).

Table 4: Transitions of organic species observed for northern IRDCs.

Molecule	Transition	Rest frequency (MHz)	A ($\times 10^{-5} \text{ s}^{-1}$)	g_u	E_{up}/k (K)	Telescope	Beam ($''$)
CH ₃ OH	5 ₀₅ -4 ₁₃ E	76509.6	0.089	11	47.93	IRAM	33
CH ₃ CHO	4 ₀₄ -3 ₀₃ E	76866.4	1.485	18	9.32	IRAM	33
CH ₃ CHO	4 ₀₄ -3 ₀₃ A++	76878.9	1.485	18	9.23	IRAM	33
CH ₃ OCH ₃	9 ₀₉ -8 ₁₈ AA	153054.49	2.191	190	40.39	IRAM	16
CH ₃ OCH ₃	9 ₀₉ -8 ₁₈ EE	153054.84	2.191	304	40.39	IRAM	16
CH ₃ OCH ₃	9 ₀₉ -8 ₁₈ AE	153055.18	2.191	114	40.39	IRAM	16
CH ₃ OCH ₃	9 ₀₉ -8 ₁₈ EA	153055.19	2.191	76	40.39	IRAM	16
CH ₃ CCH	9 ₃ -8 ₃	153790.7	1.095	76	101.93	IRAM	16
CH ₃ CCH	9 ₂ -8 ₂	153805.4	1.171	38	65.81	IRAM	16
CH ₃ CCH	9 ₁ -8 ₁	153814.2	1.217	38	44.13	IRAM	16
CH ₃ CCH	9 ₀ -8 ₀	153817.2	1.233	38	36.91	IRAM	16
HNCO	7 ₀₇ -6 ₀₆	153865.09	4.939	15	29.53	IRAM	16
CH ₃ OH	1 _{1,0} - 0 _{0,0} E	213427.1	3.370	3	23.36	APEX	~30
H ₂ CO	3 _{0,3} - 2 _{0,2}	218222.2	28.177	7	20.95	APEX	~29
H ₂ CO	3 _{2,2} - 2 _{2,1}	218475.6	15.714	7	68.09	APEX	~29
H ₂ CO	3 _{2,1} - 2 _{2,0}	218760.0	15.776	7	68.11	APEX	~29
CH ₃ OH	4 _{2,2} - 3 _{1,2} E	218440.0	4.687	9	45.45	APEX	~29
C ¹⁸ O	2-1	219560.3	0.0601	5	15.80	APEX	~29

Notes: Einstein A coefficients, degeneracy, and lower state energy levels for CH₃CHO taken from JPL data base (<http://spec.jpl.nasa.gov>), for all other molecules from CDMS Catalog (<http://www.astro.uni-koeln.de/cdms/catalog>).

Table 5: Transitions of organic species detected with IRAM telescope only in IRDC028.34-6.

Molecule	Transition	Rest frequency (MHz)	A ($\times 10^{-5} \text{ s}^{-1}$)	g_u	E_{up}/k (K)
CH ₃ OH	12 _{0,12} -12 _{-1,12} E	153281.207	1.288	25	193.78
CH ₃ OH	11 _{0,11} -11 _{-1,11} E	154425.765	1.422	23	166.04
CH ₃ OH	10 _{0,10} -10 _{-1,10} E	155320.834	1.549	21	140.60
CH ₃ OH	9 _{0,9} -9 _{-1,9} E	155997.472	1.671	19	117.45
CH ₃ CHO	4 _{2,2} -3 _{2,1} A++	77218.29	1.642	18	18.32
CH ₃ CHO	4 _{2,3} -3 _{2,2} A-	77038.6	1.634	18	18.31
CH ₃ CHO	4 _{2,2} -3 _{2,1} E	77125.69	1.636	18	18.39
CH ₃ CHO	8 _{0,8} -7 _{0,7} A++	152635.19	16.353	34	33.10
CH ₃ CHO	8 _{2,7} -7 _{2,6} A-	153872.68	15.139	34	42.32
CH ₃ CHO	8 _{4,5} -7 _{4,4} A-	154200.91	11.117	34	69.48
CH ₃ CHO	8 _{2,6} -7 _{2,5} A++	155342.08	15.424	34	42.50
CH ₃ OCHO	7 _{1,7} -6 _{1,6} A	78481.388	0.712	30	15.84
CH ₃ OCHO	12 _{3,9} -11 _{3,8} E	154984.4	4.081	50	53.20
CH ₃ OCHO	12 _{3,9} -11 _{3,8} A	155002.32	4.081	50	53.19

Notes: Einstein A coefficients, degeneracy, and lower state energy levels for CH₃CHO and CH₃OCHO taken from JPL data base (<http://spec.jpl.nasa.gov>), for all other molecules from CDMS Catalog (<http://www.astro.uni-koeln.de/cdms/catalog>).

Table 6. Abundances estimated for southern IRDCs.

Name	CO ^a	CO ^b	HNCO ^c	H ₂ CO ^d	CH ₃ OH ^e [T _{EX}]	CH ₃ CCH [T _{EX}]	category ^g
IRDC309.13-1	1.4(-04)	3.6(-04)		7.6(-10)	7.2(-09) ^f		M
IRDC309.13-2	2.0(-04)	n/a					M
IRDC309.13-3	3.7(-04)	n/a					A
IRDC309.37-1	2.7(-04)	6.8(-04)	3.7(-09)	1.7(-09)			A
IRDC309.37-2	1.3(-04)	n/a			6.1(-09) ^f		A
IRDC309.37-3	2.5(-04)	6.6(-04)					Q
IRDC309.94-1	9.3(-05)	1.5(-04)	7.3(-10)	1.3(-09)	1.3(-08) ^f		A
IRDC310.39-1	2.8(-04)	n/a	3.5(-10)	1.2(-09)	1.7(-08) ^f		A, SiO
IRDC310.39-2	2.6(-04)	4.1(-04)					A
IRDC313.72-1	2.8(-04)	4.9(-04)	2.1(-09)	1.6(-09)	4.7(-08) ^f		A, SiO
IRDC313.72-2	2.9(-04)	3.6(-04)	1.7(-09)	1.1(-09)	3.3(-08) ^f		A, SiO
IRDC313.72-3	2.6(-04)	6.5(-04)	1.9(-09)	6.1(-10)	2.8(-08) ^f		Q, SiO
IRDC313.72-4	3.2(-04)	6.4(-04)					Q, SiO
IRDC316.72-1	3.6(-04)	7.0(-04)	1.4(-09)	1.8(-09)		8.1(-09)	M
IRDC316.72-2	2.2(-04)	3.4(-04)		5.1(-10)		7.6(-09)	Q
IRDC316.76-1	1.8-3.3(-04)	2.4-6.7(-04)	1.5-3.1(-09)	7.0-30.0(-10)	8.6-14.0(-09) ^f	1.5(-08)	A, SiO
IRDC316.76-1						[38 K]	A, SiO
IRDC316.76-2	1.7-5.1(-04)	1.8-9.4(-04)		5.4-56.2(-10)	5.2(-10)	1.7-11.0(-09)	A
IRDC316.76-2					[52.8 K]		A
IRDC317.71-1	1.5(-04)	3.2(-04)	8.1(-10)				Q
IRDC317.71-2	7.3(-05)	1.1(-04)	5.3(-10)	2.8(-10)	4.5(-09)	3.4(-09)	A
IRDC317.71-2					[12.4 K]	[17 K]	A
IRDC317.71-3	2.7(-04)	6.4(-04)					Q, SiO
IRDC321.73-1	1.1(-04)	2.4(-04)		1.1(-09)	6.5(-08)		M, SiO
IRDC321.73-1					[12.2 K]		M, SiO
IRDC321.73-2	6.9(-05)	1.4(-04)		2.6(-10)	4.2(-09) ^f		M
IRDC321.73-3	8.2(-05)	1.3(-04)					A
IRDC013.90-1	9.7(-05)	1.9(-04)		2.0(-10)			M
IRDC013.90-2	2.2(-04)	1.8(-04)					Q
Detection rates	100%	100%	40%	60%	48%	20%	

Note. — a(b) = a×10^b. Blank spaces indicate non-detections and n/a indicates absence of data

^aCO abundance estimated based on C¹⁸O(2-1) APEX data.

^bCO abundance estimated based on C¹⁸O(1-0) Mopra data.

^cHNCO data taken from Vasyunina et al. (2011).

^dH₂CO abundance estimated based on H₂CO(3_{0,3}-2_{0,2}) APEX data.

^eCH₃OH abundance estimated based on APEX data.

^fAbundances calculated based on CH₃OH 5_{-1,5} - 4_{-1,4} E transition.

^gMIR categories; see Table 1.

Table 7. Abundances estimated for northern IRDCs.

Name	CO ^a	HNCO	H ₂ CO ^b	CH ₃ OH [T _{ex}]	CH ₃ CCH [T _{ex}]	CH ₃ CHO [T _{ex}]	CH ₃ OCH ₃	category ^f
IRDC010.70-2	0.9-2.7(-04)	1.2-3.2(-10)	6.3-25.1(-10)	4.8-9.8(-09) ^e	0.6-1.3(-09)	1.9-10.3(-09)		A,SiO
IRDC010.70-4	1.4-3.9(-04)	0.9-2.4(-10)	4.5-16.0(-10)		4.2±1.5(-09)			A,SiO
IRDC010.70-4					[42±13 K]			
IRDC011.11-2	0.7-2.6(-04)	0.5-1.4(-10)	1.4-6.3(-10)		0.5-1.1(-09)	0.4-2.5(-09)	<2.4(-09)	Q,SiO
IRDC011.11-4	0.7-2.5(-04)	1.3-4.0(-10)	4.1-20.8(-10)	3.6-7.4(-09) ^e	4.5±0.8(-09)	0.4-2.9(-09)		A,SiO
IRDC011.11-4					[28±2 K]			
IRDC011.11-5	0.5-3.0(-04)	0.3-1.0(-10)	0.3-3.0(-10)					Q
IRDC013.90-1	1.0-4.0(-04)	0.4-1.2(-10)	2.8-14.4(-10)		1.7±0.3(-09)		<1.4(-09)	Q/M
IRDC013.90-1					[27±3 K]			
IRDC015.05-2	1.0-5.4(-04)	1.2-4.0(-10)	1.6-13.5(-10)		1.7-3.7(-09)	0.2-3.4(-09)		Q,SiO
IRDC015.05-3	1.8-3.6(-04)	1.6-2.8(-10)	6.1-14.0(-10)	4.1-5.8(-09) ^e	0.9-1.4(-09)	1.2-3.3(-09)		Q
IRDC018.48-7	0.7-3.9(-04)	0.3-0.9(-10)	0.6-5.1(-10)		0.6-1.3(-09)			M
IRDC018.48-8	1.6-8.6(-04)		2.9-23.7(-10)		1.9-4.1(-09)			Q,SiO
IRDC019.30-1	1.4-3.4(-04)	4.3-11.3(-10)	16.9-66.7(-10)	7.3±0.6(-08) ^c	5.7±0.9(-09)	2.3-12.2(-09)	<3.8(-09)	A,SiO
IRDC019.30-1				[25±1 K]	[34±4 K]			
IRDC028.34-3	1.0-4.3(-04)	1.3-3.6(-10)	13.8-55.5(-10)	1.2-2.7(-08) ^e	4.4±0.7(-09)	2.5-13.3(-09)	<4.5(-09)	M,SiO
IRDC028.34-3					[32±4 K]			
IRDC028.34-4	1.0-2.5(-04)	0.9-1.9(-10)	2.2-7.1(-10)		0.3-0.5(-09)			M,SiO?
IRDC028.34-6	0.6-2.1(-04)	2.0-5.8(-10)	7.3-31.3(-10)	1.4±0.1(-08) ^d	3.4±0.2(-09)	1.1±0.1(-09)	<1.9(-09)	A,SiO
IRDC028.34-6				[43±1 K]	[36±2 K]	[23±1 K]		
IRDC048.66-1	0.9-5.1(-04)		2.6-21.8(-10)		2.2±1.1(-09)			A,SiO
IRDC048.66-1					[30±9 K]			
IRDC048.66-3	0.7-3.7(-04)	0.7-2.3(-10)	2.5-20.8(-10)			0.7-9.5(-09)		Q,SiO
IRDC079.31-2	0.1-0.6(-04)	0.1-0.4(-10)	0.8-4.7(-10)		0.1-0.3(-09)	0.1-0.8(-09)		Q
ISOSSJ23053	n/a	1.0-1.1(-10)	n/a		4.0±0.9(-09)	0.5-0.7(-09)		M
ISOSSJ23053					[31±1 K]			
Detection rates	100%	89%	100%	33%	89%	61%	28%	

Note. — a(b) = a×10^b. Blank spaces indicate non-detections and n/a indicates absence of data

^aCO abundance estimated based on C¹⁸O(2-1) APEX data.

^bH₂CO abundance estimated based on H₂CO(3_{0,3}-2_{0,2}) APEX data.

^cCH₃OH abundance estimated based on He et al. (2012) data and APEX data from the current survey.

^dCH₃OH abundance estimated based on APEX and IRAM data.

^eAbundances calculated based on CH₃OH 4_{2,2} - 3_{1,2} E transition.

^fMIR categories; See Table 1.

Table 8. Line parameters for southern IRDCs.

Name	$\int T_A dv$ (K km/s)	V_{lsr} km/s	ΔV km/s	T_A K	1σ rms K
CH ₃ OH 5 _{-1,5} -4 _{0,4} E					
IRDC309.13-1	n/a				
IRDC309.13-2	n/a				
IRDC309.13-3	n/a				
IRDC309.37-1	n/a				
IRDC309.37-2	n/a				
IRDC309.37-3	n/a				
IRDC309.94-1	1.7 (0.04)	-60.3 (0.03)	3.3 (0.09)	0.49	2.8 (-02)
IRDC310.39-1	n/a				
IRDC310.39-2	0.3 (0.04)	-54.1 (0.04)	1.1 (0.20)	0.31	3.1 (-02)
IRDC313.72-1	n/a				
IRDC313.72-2	n/a				
IRDC313.72-3	n/a				
IRDC313.72-4	n/a				
IRDC316.72-1					2.2 (-02)
IRDC316.72-2					2.2 (-02)
IRDC316.76-1	0.6 (0.04)	-39.2 (0.13)	3.7 (0.35)	0.15	3.0 (-02)
IRDC316.76-2	0.6 (0.05)	-39.3 (0.13)	3.1 (0.36)	0.18	4.0 (-02)
IRDC317.71-1	n/a				
IRDC317.71-2	n/a				
IRDC317.71-3	n/a				
IRDC321.73-1	1.2 (0.03)	-32.2 (0.03)	2.5 (0.08)	0.46	3.9 (-02)
IRDC321.73-2	n/a				
IRDC321.73-3	n/a				
IRDC013.90-1					2.4 (-02)
C ¹⁸ O 1-0					
IRDC309.13-1	2.0 (0.07)	-45.1 (0.03)	2.2 (0.09)	0.87	6.7 (-02)
IRDC309.13-2	n/a				
IRDC309.13-3	n/a				
IRDC309.37-1	3.3 (0.07)	-42.6 (0.03)	3.0 (0.07)	1.01	6.8 (-02)
IRDC309.37-2	n/a				
IRDC309.37-3	3.8 (0.07)	-41.9 (0.02)	2.7 (0.06)	1.32	6.9 (-02)
IRDC309.94-1	3.1 (0.09)	-59.2 (0.04)	3.1 (0.12)	0.94	7.2 (-02)
IRDC310.39-1	n/a				
IRDC310.39-2	3.0 (0.05)	-52.5 (0.00)	2.2 (0.04)	1.31	5.9 (-02)
IRDC313.72-1	1.5 (0.07)	-43.8 (0.05)	2.2 (0.11)	0.63	5.9 (-02)
IRDC313.72-2	1.2 (0.08)	-44.1 (0.05)	1.8 (0.12)	0.63	6.1 (-02)
IRDC313.72-3	1.7 (0.06)	-44.0 (0.03)	2.2 (0.09)	0.72	4.9 (-02)
IRDC313.72-4	0.40 (0.05)	-44.8 (0.03)	0.8 (0.12)	0.42	5.2 (-02)
IRDC316.72-1	4.8 (0.06)	-39.5 (0.01)	2.7 (0.04)	1.66	5.5 (-02)
IRDC316.72-2	2.8 (0.04)	-39.4 (0.01)	1.6 (0.03)	1.59	5.6 (-02)
IRDC316.76-1	6.5 (0.06)	-41.2 (0.01)	2.8 (0.03)	2.14	6.1 (-02)
IRDC316.76-2	5.7 (0.06)	-41.2 (0.01)	2.9 (0.03)	1.82	6.1 (-02)
IRDC317.71-1	3.3 (0.07)	-43.6 (0.03)	2.6 (0.08)	1.17	6.7 (-02)
IRDC317.71-2	3.3 (0.07)	-44.1 (0.02)	1.9 (0.06)	1.56	7.6 (-02)

Table 8—Continued

Name	$\int T_A dv$ (K km/s)	V_{lsr} km/s	ΔV km/s	T_A K	1σ rms K
IRDC317.71-3	3.3 (0.09)	-44.1 (0.03)	2.9 (0.11)	1.06	7.8 (-02)
IRDC321.73-1	1.8 (0.10)	-32.1 (0.05)	2.2 (0.20)	0.77	7.2 (-02)
IRDC321.73-2	2.3 (0.07)	-32.9 (0.04)	2.5 (0.10)	0.87	7.2 (-02)
IRDC321.73-3	2.5 (0.09)	-32.3 (0.06)	3.2 (0.15)	0.71	8.3 (-02)
IRDC013.90-1	4.4 (0.08)	23.6 (0.02)	2.9 (0.06)	1.42	6.5 (-02)
C ¹⁷ O 1-0					
IRDC309.13-1					7.4 (-02)
IRDC309.13-2	n/a				
IRDC309.13-3	n/a				
IRDC309.37-1	0.8 (0.13)	-41.6 (0.30)	4.8 (1.00)	0.17	8.1 (-02)
IRDC309.37-2	n/a				
IRDC309.37-3	1.2 (0.10)	-42.0 (0.20)	4.0 (0.39)	0.27	8.5 (-02)
IRDC309.94-1	0.5 (0.10)	-59.0 (0.21)	2.5 (0.70)	0.20	9.1 (-02)
IRDC310.39-1	n/a				
IRDC310.39-2	0.6 (0.08)	-52.5 (0.29)	4.4 (0.58)	0.14	6.3 (-02)
IRDC313.72-1	0.7 (0.09)	-42.8 (0.33)	5.1 (0.69)	0.13	6.6 (-02)
IRDC313.72-2					7.0 (-02)
IRDC313.72-3					5.9 (-02)
IRDC313.72-4					6.1 (-02)
IRDC316.72-1	0.8 (0.08)	-38.6 (0.11)	2.6 (0.32)	0.30	6.6 (-02)
IRDC316.72-2	0.4 (0.06)	-38.3 (0.09)	1.6 (0.28)	0.26	6.5 (-02)
IRDC316.76-1	1.0 (0.09)	-40.5 (0.10)	2.7 (0.37)	0.35	6.8 (-02)
IRDC316.76-2	1.3 (0.09)	-40.9 (0.15)	4.2 (0.32)	0.29	7.2 (-02)
IRDC317.71-1	0.4 (0.07)	-43.1 (0.08)	1.3 (0.31)	0.32	7.7 (-02)
IRDC317.71-2	0.7 (0.06)	-43.4 (0.06)	1.4 (0.14)	0.48	8.3 (-02)
IRDC317.71-3	0.7 (0.11)	-43.2 (0.15)	2.3 (0.49)	0.29	9.3 (-02)
IRDC321.73-1					7.6 (-02)
IRDC321.73-2					8.4 (-02)
IRDC321.73-3					9.8 (-02)
IRDC013.90-1	1.4 (0.11)	22.6 (0.24)	6.4 (0.49)	0.21	7.2 (-02)
CH ₃ OH 1 _{1,0} -0 _{0,0} E					
IRDC309.13-1	0.13 (0.03)	-44.8 (0.14)	0.8 (0.24)	0.13	4.6 (-02)
IRDC309.13-2	n/a				
IRDC309.13-3					7.6 (-02)
IRDC309.37-1					7.6 (-02)
IRDC309.37-2					8.4 (-02)
IRDC309.37-3	n/a				
IRDC309.94-1	0.46 (0.07)	-59.5 (0.18)	2.3 (0.34)	0.19	6.9 (-02)
IRDC310.39-1					7.6 (-02)
IRDC310.39-2					7.6 (-02)
IRDC313.72-1					7.3 (-02)
IRDC313.72-2					7.8 (-02)
IRDC313.72-3					8.2 (-02)
IRDC313.72-4					7.2 (-02)
IRDC316.72-1					7.6 (-02)

Table 8—Continued

Name	$\int T_A dv$ (K km/s)	V_{lsr} km/s	ΔV km/s	T_A K	1σ rms K
IRDC316.72-2					5.6 (-02)
IRDC316.76-1	0.37 (0.06)	-40.0 (0.25)	2.7 (0.60)	0.12	5.3 (-02)
IRDC316.76-2					7.9 (-02)
IRDC317.71-1					7.3 (-02)
IRDC317.71-2	1.12 (0.13)	-44.4 (0.33)	5.5 (0.83)	0.19	8.2 (-02)
IRDC317.71-3					8.0 (-02)
IRDC321.73-1	0.74 (0.11)	-32.3 (0.26)	3.3 (0.52)	0.20	9.1 (-02)
IRDC321.73-2					9.3 (-02)
IRDC321.73-3					9.2 (-02)
IRDC013.90-1					9.2 (-02)
H_2CO $3_{0,3} - 2_{0,2}$					
IRDC309.13-1	1.0 (0.12)	-43.9 (0.31)	5.5 (0.82)	0.17	0.07
IRDC309.13-2					
IRDC309.13-3					
IRDC309.37-1	1.9 (0.08)	-42.9 (0.05)	2.9 (0.16)	0.62	0.06
IRDC309.37-2					
IRDC309.37-3					
IRDC309.94-1	4.6 (0.15)	-59.7 (0.06)	3.7 (0.16)	1.17	0.10
IRDC310.39-1	2.2 (0.13)	-53.3 (0.09)	3.5 (0.23)	0.60	0.10
IRDC310.39-2					
IRDC313.72-1	1.5 (0.14)	-44.8 (0.15)	3.3 (0.36)	0.42	0.10
IRDC313.72-2	1.0 (0.11)	-44.6 (0.14)	2.7 (0.37)	0.35	0.09
IRDC313.72-3	0.4 (0.07)	-43.9 (0.09)	1.2 (0.19)	0.37	0.10
IRDC313.72-4					
IRDC316.72-1	2.6 (0.22)	-38.7 (0.23)	6.2 (0.74)	0.40	0.11
IRDC316.72-2	0.8 (0.11)	-40.1 (0.13)	1.9 (0.39)	0.40	0.10
IRDC316.76-1	3.9 (0.14)	-40.1 (0.07)	4.2 (0.19)	0.87	0.10
IRDC316.76-2	3.8 (0.13)	-41.0 (0.04)	2.7 (0.11)	1.30	0.10
IRDC317.71-1					
IRDC317.71-2	2.1 (0.14)	-44.3 (0.09)	3.0 (0.26)	0.66	0.10
IRDC317.71-3					
IRDC321.73-1	2.1 (0.10)	-32.7 (0.05)	2.3 (0.13)	0.87	0.10
IRDC321.73-2	0.9 (0.13)	-34.5 (0.18)	2.6 (0.49)	0.35	0.11
IRDC321.73-3					
IRDC013.90-1	1.1 (0.09)	23.3 (0.11)	2.7 (0.26)	0.39	0.08
H_2CO $3_{2,2} - 2_{2,1}$					
IRDC309.13-1					7.3 (-02)
IRDC309.13-2					9.7 (-02)
IRDC309.13-3					0.1
IRDC309.37-1	0.2 (0.04)	-42.8 (0.16)	1.3 (0.37)	0.12	5.7 (-02)
IRDC309.37-2					9.4 (-02)
IRDC309.37-3					9.8 (-02)
IRDC309.94-1	1.0 (0.14)	-59.8 (0.22)	3.1 (0.53)	0.30	9.8 (-02)
IRDC310.39-1					9.6 (-02)
IRDC310.39-2					9.4 (-02)

Table 8—Continued

Name	$\int T_A dv$ (K km/s)	V_{lsr} km/s	ΔV km/s	T_A K	1σ rms K
IRDC313.72-1					0.1
IRDC313.72-2					9.7 (-02)
IRDC313.72-3					0.1
IRDC313.72-4					0.1
IRDC316.72-1					4.4 (-02)
IRDC316.72-2					4.6 (-02)
IRDC316.76-1	1.0 (0.07)	-39.5 (0.17)	4.9 (0.42)	0.19	4.5 (-02)
IRDC316.76-2	0.5 (0.06)	-40.8 (0.13)	2.7 (0.42)	0.19	4.7 (-02)
IRDC317.71-1					4.7 (-02)
IRDC317.71-2	0.3 (0.06)	-44.1 (0.21)	2.4 (0.84)	0.11	4.5 (-02)
IRDC317.71-3					4.9 (-02)
IRDC321.73-1	0.7 (0.06)	-32.4 (0.12)	3.0 (0.32)	0.22	4.9 (-02)
IRDC321.73-2					9.5 (-02)
IRDC321.73-3					9.8 (-02)
IRDC013.90-1					
H ₂ CO 3 _{2,1} - 2 _{2,0}					
IRDC309.13-1					7.3 (-02)
IRDC309.13-2					9.7 (-02)
IRDC309.13-3					0.1
IRDC309.37-1					6.4 (-02)
IRDC309.37-2					9.4 (-02)
IRDC309.37-3					9.8 (-02)
IRDC309.94-1	1.0 (0.11)	-59.5 (0.14)	2.5 (0.32)	0.37	0.1
IRDC310.39-1					9.6 (-02)
IRDC310.39-2					9.4 (-02)
IRDC313.72-1					0.1
IRDC313.72-2					9.7 (-02)
IRDC313.72-3					0.1
IRDC313.72-4					0.1
IRDC316.72-1					4.4 (-02)
IRDC316.72-2					4.6 (-02)
IRDC316.76-1	1.0 (0.08)	-39.5 (0.21)	5.4 (0.52)	0.17	4.7 (-02)
IRDC316.76-2	0.5 (0.05)	-40.9 (0.12)	2.8 (0.37)	0.19	4.6 (-02)
IRDC317.71-1					4.7 (-02)
IRDC317.71-2	0.3 (0.05)	-43.0 (0.28)	3.6 (0.49)	0.1	4.6 (-02)
IRDC317.71-3					4.9 (-02)
IRDC321.73-1	0.7 (0.05)	-32.5 (0.09)	2.5 (0.22)	0.26	4.9 (-02)
IRDC321.73-2					9.5 (-02)
IRDC321.73-3					9.8 (-02)
IRDC013.90-1					
CH ₃ OH 4 _{2,2} -3 _{1,2} E					
IRDC309.13-1					7.3 (-02)
IRDC309.13-2					9.7 (-02)
IRDC309.13-3					0.1
IRDC309.37-1					6.4 (-02)

Table 8—Continued

Name	$\int T_A dv$ (K km/s)	V_{lsr} km/s	ΔV km/s	T_A K	1σ rms K
IRDC309.37-2					9.4 (-02)
IRDC309.37-3					9.8 (-02)
IRDC309.94-1	0.9 (0.10)	-59.9 (0.14)	2.5 (0.32)	0.35	0.1
IRDC310.39-1	0.7 (0.14)	-53.7 (0.26)	3.1 (0.89)	0.21	9.6 (-02)
IRDC310.39-2					9.4 (-02)
IRDC313.72-1					0.1
IRDC313.72-2					9.7 (-02)
IRDC313.72-3					0.1
IRDC313.72-4					0.1
IRDC316.72-1					4.4 (-02)
IRDC316.72-2					4.6 (-02)
IRDC316.76-1	0.8 (0.08)	-39.8 (0.15)	3.4 (0.48)	0.22	4.5 (-02)
IRDC316.76-2	0.4 (0.06)	-40.1 (0.19)	2.8 (0.48)	0.14	5.4 (-02)
IRDC317.71-1					4.7 (-02)
IRDC317.71-2	0.5 (0.06)	-44.3 (0.17)	3.1 (0.47)	0.17	5.1 (-02)
IRDC317.71-3					4.9 (-02)
IRDC321.73-1	1.0 (0.06)	-32.4 (0.07)	2.2 (0.18)	0.41	5.0 (-02)
IRDC321.73-2					9.5 (-02)
IRDC321.73-3					9.8 (-02)
IRDC013.90-1					
C ¹⁸ O 2-1					
IRDC309.13-1	3.3 (0.08)	-45.1 (0.02)	1.9 (0.06)	1.59	6.6 (-02)
IRDC309.13-2	3.6 (0.11)	-44.9 (0.04)	2.8 (0.10)	1.23	9.9 (-02)
IRDC309.13-3	4.6 (0.29)	-45.3 (0.07)	2.3 (0.15)	1.86	0.1
IRDC309.37-1	7.0 (0.07)	-42.4 (0.01)	3.0 (0.03)	2.16	6.0 (-02)
IRDC309.37-2	4.5 (0.19)	-48.8 (0.07)	3.3 (0.15)	1.25	0.1
IRDC309.37-3	5.7 (0.10)	-42.0 (0.02)	2.4 (0.05)	2.21	9.6 (-02)
IRDC309.94-1	10. (0.12)	-59.3 (0.01)	2.8 (0.04)	3.42	9.4 (-02)
IRDC310.39-1	10. (0.10)	-52.7 (0.01)	2.5 (0.02)	3.94	9.4 (-02)
IRDC310.39-2	10. (0.11)	-52.4 (0.01)	2.7 (0.03)	3.44	9.7 (-02)
IRDC313.72-1	2.1 (0.11)	-44.0 (0.04)	1.8 (0.10)	1.07	9.7 (-02)
IRDC313.72-2	2.4 (0.10)	-44.1 (0.04)	2.0 (0.10)	1.11	9.7 (-02)
IRDC313.72-3	1.7 (0.09)	-43.9 (0.04)	1.6 (0.09)	0.99	9.5 (-02)
IRDC313.72-4	1.0 (0.37)	-44.5 (0.09)	1.8 (0.24)	0.54	9.4 (-02)
IRDC316.72-1	13. (0.05)	-39.9 (0.00)	3.2 (0.01)	3.73	4.3 (-02)
IRDC316.72-2	9.6 (0.04)	-39.6 (0.00)	1.9 (0.01)	4.66	4.7 (-02)
IRDC316.76-1	23. (0.05)	-41.0 (0.00)	3.4 (0.00)	6.37	4.2 (-02)
IRDC316.76-2	25. (0.10)	-41.0 (0.00)	2.9 (0.01)	8.02	4.5 (-02)
IRDC317.71-1	5.8 (0.05)	-43.9 (0.01)	2.7 (0.03)	2.00	4.3 (-02)
IRDC317.71-2	8.5 (0.05)	-44.3 (0.00)	2.8 (0.02)	2.85	4.4 (-02)
IRDC317.71-3	5.2 (0.05)	-44.4 (0.01)	2.5 (0.03)	1.93	4.8 (-02)
IRDC321.73-1	3.6 (0.06)	-32.3 (0.01)	1.8 (0.04)	1.82	4.5 (-02)
IRDC321.73-2	3.0 (0.10)	-33.5 (0.02)	1.5 (0.06)	1.86	0.1
IRDC321.73-3	3.9 (0.13)	-32.4 (0.05)	3.2 (0.11)	1.14	0.1
IRDC013.90-1					

Table 8—Continued

Name	$\int T_A dv$ (K km/s)	V_{lsr} km/s	ΔV km/s	T_A K	1σ rms K
CH ₃ OH 5 _{0,5} -4 _{0,4} E					
IRDC309.13-1					9.3 (-02)
IRDC309.13-2					9.9 (-02)
IRDC309.13-3	n/a				
IRDC309.37-1					9.8 (-02)
IRDC309.37-2					0.1
IRDC309.37-3					0.1
IRDC309.94-1					0.1
IRDC310.39-1					0.1
IRDC310.39-2					0.1
IRDC313.72-1					0.1
IRDC313.72-2					0.1
IRDC313.72-3					0.1
IRDC313.72-4					0.1
IRDC316.72-1					0.1
IRDC316.72-2					0.1
IRDC316.76-1	0.75 (0.12)	-39.4 (0.26)	3.0 (0.53)	0.23	0.1
IRDC316.76-2					0.1
IRDC317.71-1					0.1
IRDC317.71-2					0.1
IRDC317.71-3					0.1
IRDC321.73-1	1.2 (0.12)	-32.6 (0.12)	2.7 (0.33)	0.42	0.1
IRDC321.73-2					0.1
IRDC321.73-3					0.1
IRDC013.90-1					0.1
CH ₃ OH 5 _{-1,5} -4 _{-1,4} E					
IRDC309.13-1	0.37 (0.07)	-44.6 (0.13)	1.2 (0.31)	0.28	9.6 (-02)
IRDC309.13-2					9.9 (-02)
IRDC309.13-3	n/a				
IRDC309.37-1					9.8 (-02)
IRDC309.37-2	0.39 (0.09)	-49.2 (0.16)	1.4 (0.49)	0.24	0.1
IRDC309.37-3					0.1
IRDC309.94-1	4.0 (0.32)	-59.6 (0.11)	3.1 (0.31)	1.23	0.1
IRDC310.39-1	1.8 (0.24)	-53.1 (0.19)	3.1 (0.53)	0.55	7.6 (-02)
IRDC310.39-2					0.1
IRDC313.72-1	1.8 (0.21)	-44.3 (0.20)	4.0 (0.66)	0.41	0.1
IRDC313.72-2	1.3 (0.16)	-44.6 (0.18)	3.2 (0.48)	0.39	0.1
IRDC313.72-3	0.87 (0.15)	-42.5 (0.46)	5.1 (1.00)	0.15	0.1
IRDC313.72-4					0.1
IRDC316.72-1					0.1
IRDC316.72-2					0.1
IRDC316.76-1	2.9 (0.29)	-39.9 (0.21)	4.7 (0.58)	0.59	0.1
IRDC316.76-2	1.2 (0.14)	-40.7 (0.18)	3.1 (0.45)	0.36	0.1
IRDC317.71-1					0.1
IRDC317.71-2	1.5 (0.13)	-44.1 (0.09)	2.2 (0.24)	0.64	0.1

Table 8—Continued

Name	$\int T_A dv$ (K km/s)	V_{lsr} km/s	ΔV km/s	T_A K	1σ rms K
IRDC317.71-3					0.1
IRDC321.73-1	3.4 (0.28)	-32.4 (0.09)	2.2 (0.22)	1.43	0.1
IRDC321.73-2	0.37 (0.09)	-34.1 (0.20)	1.5 (0.33)	0.23	0.1
IRDC321.73-3					0.1
IRDC013.90-1					0.1
CH ₃ OH 5 _{0,5} -4 _{0,4} A+					
IRDC309.13-1					9.3 (-02)
IRDC309.13-2					9.9 (-02)
IRDC309.13-3	n/a				
IRDC309.37-1					9.8 (-02)
IRDC309.37-2					0.1
IRDC309.37-3					0.1
IRDC309.94-1	5.1 (0.29)	-59.6 (0.08)	3.2 (0.24)	1.47	0.1
IRDC310.39-1	2.7 (0.22)	-53.0 (0.13)	3.6 (0.39)	0.70	7.6 (-02)
IRDC310.39-2					0.1
IRDC313.72-1	2.6 (0.21)	-44.1 (0.18)	4.9 (0.55)	0.50	0.1
IRDC313.72-2	1.7 (0.16)	-44.3 (0.14)	3.4 (0.44)	0.47	0.1
IRDC313.72-3	0.89 (0.13)	-43.1 (0.28)	3.7 (0.59)	0.22	0.1
IRDC313.72-4					0.1
IRDC316.72-1					0.1
IRDC316.72-2					0.1
IRDC316.76-1	3.5 (0.23)	-39.7 (0.12)	3.9 (0.32)	0.84	0.1
IRDC316.76-2	1.2 (0.12)	-40.9 (0.13)	2.5 (0.30)	0.45	0.1
IRDC317.71-1					0.1
IRDC317.71-2	1.6 (0.15)	-44.0 (0.11)	2.5 (0.29)	0.59	0.1
IRDC317.71-3					0.1
IRDC321.73-1	5.0 (0.23)	-32.3 (0.05)	2.5 (0.14)	1.86	0.1
IRDC321.73-2	0.69 (0.12)	-35.1 (0.28)	2.8 (0.58)	0.22	0.1
IRDC321.73-3					0.1
IRDC013.90-1					0.1

Note. — Blank spaces indicate non-detections and n/a indicates absence of data

Table 9. Line parameters for northern IRDCs.

Name	$\int T_A dv$ (K km/s)	V_{lsr} km/s	ΔV km/s	T_A K	1σ rms K
CH ₃ OH 5 _{0,5} -4 _{1,3} E					
IRDC010.70-2					2.8 (-02)
IRDC010.70-4					2.9 (-02)
IRDC011.11-2					1.4 (-02)
IRDC011.11-4	0.2 (0.07)	29.8 (0.70)	5.3 (1.96)	4.73(-02)	1.7 (-02)
IRDC011.11-5					1.3 (-02)
IRDC013.90-1					1.4 (-02)
IRDC015.05-2					1.4 (-02)
IRDC015.05-3					1.8 (-02)
IRDC018.48-7					1.3 (-02)
IRDC018.48-8					1.5 (-02)
IRDC019.30-1	0.3 (0.05)	26.2 (0.33)	4.3 (0.87)	7.31(-02)	1.7 (-02)
IRDC028.34-3	0.3 (0.05)	79.4 (0.57)	6.7 (1.28)	4.22(-02)	1.5 (-02)
IRDC028.34-4					1.5 (-02)
IRDC028.34-6	0.8 (0.04)	77.8 (0.11)	4.1 (0.33)	0.18	1.6 (-02)
IRDC048.66-1					2.6 (-02)
IRDC048.66-3					1.3 (-02)
IRDC079.31-2					1.4 (-02)
ISOSSJ23053					1.2 (-02)
CH ₃ CHO 4 _{0,4} -3 _{0,3} E					
IRDC010.70-2	0.2 (0.06)	29.1 (0.30)	2.3 (0.64)	0.11	3.1 (-02)
IRDC010.70-4					3.3 (-02)
IRDC011.11-2					1.6 (-02)
IRDC011.11-4	0.2 (0.07)	30.2 (0.57)	3.7 (1.41)	5.73(-02)	1.8 (-02)
IRDC011.11-5					1.4 (-02)
IRDC013.90-1					1.9 (-02)
IRDC015.05-2					1.5 (-02)
IRDC015.05-3	0.1 (0.05)	24.8 (0.50)	2.9 (1.27)	4.66(-02)	2.1 (-02)
IRDC018.48-7					1.3 (-02)
IRDC018.48-8					1.5 (-02)
IRDC019.30-1	0.4 (0.04)	26.0 (0.15)	3.3 (0.40)	0.13	1.9 (-02)
IRDC028.34-3	0.5 (0.06)	79.0 (0.15)	3.1 (0.38)	0.17	1.5 (-02)
IRDC028.34-4					1.5 (-02)
IRDC028.34-6	0.5 (0.06)	78.1 (0.17)	3.0 (0.45)	0.17	1.7 (-02)
IRDC048.66-1					2.5 (-02)
IRDC048.66-3	7.3E-02 (0.02)	33.1 (0.47)	2.3 (0.81)	2.94(-02)	1.3 (-02)
IRDC079.31-2					
ISOSSJ23053					1.4 (-02)
CH ₃ CHO 4 _{0,4} -3 _{0,3} A++					
IRDC010.70-2	0.4 (0.10)	28.4 (0.58)	5.3 (1.40)	7.85(-02)	3.1 (-02)
IRDC010.70-4					3.3 (-02)
IRDC011.11-2	0.1 (0.03)	30.3 (0.32)	1.7 (0.69)	6.46(-02)	1.6 (-02)
IRDC011.11-4	0.1 (0.06)	30.5 (0.66)	3.3 (1.60)	5.47(-02)	1.8 (-02)
IRDC011.11-5					1.3 (-02)
IRDC013.90-1					1.7 (-02)

Table 9—Continued

Name	$\int T_A dv$ (K km/s)	V_{lsr} km/s	ΔV km/s	T_A K	1σ rms K
IRDC015.05-2					1.5 (-02)
IRDC015.05-3	0.1 (0.04)	24.1 (0.32)	2.2 (0.72)	7.66(-02)	2.1 (-02)
IRDC018.48-7					1.3 (-02)
IRDC018.48-8					1.5 (-02)
IRDC019.30-1	0.5 (0.05)	26.2 (0.21)	4.4 (0.65)	0.11	1.8 (-02)
IRDC028.34-3	0.6 (0.06)	78.9 (0.15)	3.3 (0.38)	0.17	1.5 (-02)
IRDC028.34-4					1.5 (-02)
IRDC028.34-6	0.7 (0.07)	78.3 (0.16)	3.7 (0.54)	0.17	1.7 (-02)
IRDC048.66-1					2.5 (-02)
IRDC048.66-3	0.1 (0.02)	33.3 (0.27)	2.7 (0.59)	4.99(-02)	1.3 (-02)
IRDC079.31-2	9.7(-02)(0.03)	1.4 (0.37)	2.5 (1.24)	3.63(-02)	1.4 (-02)
ISOSSJ23053	0.0 0.0	0.0 0.0	0.0 0.0	0.0	1.4 (-02)
CH ₃ CCH 9 ₃ -8 ₃					
IRDC010.70-2					3.7 (-02)
IRDC010.70-4	8.3(-02)(0.05)	27.5 (0.91)	2.2 (1.15)	3.46(-02)	3.9 (-02)
IRDC011.11-2					1.9 (-02)
IRDC011.11-4	0.1 (0.07)	30.3 (0.49)	1.7 (0.75)	9.04(-02)	3.2 (-02)
IRDC011.11-5					1.1 (-02)
IRDC013.90-1	2.3(-02)(0.03)	23.7 (1.80)	2.1 (2.81)	1.02(-02)	1.4 (-02)
IRDC015.05-2					1.3 (-02)
IRDC015.05-3					2.5 (-02)
IRDC018.48-7					1.3 (-02)
IRDC018.48-8					1.2 (-02)
IRDC019.30-1	0.2 (0.08)	26.5 (0.85)	5.1 (2.83)	3.91(-02)	1.7 (-02)
IRDC028.34-3	0.1 (0.06)	78.6 (0.86)	3.8 (2.02)	3.65(-02)	1.8 (-02)
IRDC028.34-4					1.4 (-02)
IRDC028.34-6	0.3 (0.10)	78.0 (0.39)	2.6 (0.96)	0.12	1.5 (-02)
IRDC048.66-1	6.8(-02)(0.03)	34.8 (0.30)	1.4 (0.67)	4.55(-02)	2.2 (-02)
IRDC048.66-3					1.5 (-02)
IRDC079.31-2					1.3 (-02)
ISOSSJ23053	0.1 (0.03)	-52.1 (0.24)	1.4 (0.48)	7.10(-02)	1.2 (-02)
CH ₃ CCH 9 ₂ -8 ₂					
IRDC010.70-2					3.7 (-02)
IRDC010.70-4	0.2 (0.05)	29.2 (0.27)	1.9 (0.50)	9.95(-02)	3.9 (-02)
IRDC011.11-2					1.9 (-02)
IRDC011.11-4	0.3 (0.08)	29.5 (0.26)	1.9 (0.53)	0.14	3.2 (-02)
IRDC011.11-5					1.1 (-02)
IRDC013.90-1	0.1 (0.04)	22.7 (0.40)	2.4 (1.09)	4.46(-02)	1.4 (-02)
IRDC015.05-2					1.3 (-02)
IRDC015.05-3					2.5 (-02)
IRDC018.48-7					1.3 (-02)
IRDC018.48-8					1.2 (-02)
IRDC019.30-1	0.1 (0.05)	25.7 (0.38)	2.6 (1.21)	6.13(-02)	1.7 (-02)
IRDC028.34-3	0.1 (0.05)	78.8 (0.40)	2.1 (0.92)	5.89(-02)	1.8 (-02)
IRDC028.34-4					1.4 (-02)

Table 9—Continued

Name	$\int T_A dv$ (K km/s)	V_{lsr} km/s	ΔV km/s	T_A K	1σ rms K
IRDC028.34-6	0.5 (0.10)	77.8 (0.26)	2.8 (0.61)	0.18	1.5 (-02)
IRDC048.66-1	2.5(-02)(0.01)	34.0 (0.16)	0.4 (0.32)	4.96(-02)	2.2 (-02)
IRDC048.66-3					1.5 (-02)
IRDC079.31-2					1.3 (-02)
ISOSSJ23053	0.1 (0.04)	-51.8 (0.22)	1.8 (0.45)	8.59(-02)	1.2 (-02)
CH ₃ CCH 9 ₁ -8 ₁					
IRDC010.70-2	0.1 (0.03)	28.7 (0.07)	0.8 (0.19)	0.21	3.7 (-02)
IRDC010.70-4	0.2 (0.04)	29.0 (0.11)	1.3 (0.25)	0.19	3.9 (-02)
IRDC011.11-2	0.1 (0.02)	30.3 (0.12)	1.3 (0.26)	8.43(-02)	1.9 (-02)
IRDC011.11-4	0.8 (0.08)	29.5 (0.10)	2.3 (0.31)	0.35	3.2 (-02)
IRDC011.11-5					1.1 (-02)
IRDC013.90-1	0.2 (0.02)	22.6 (0.07)	1.6 (0.15)	0.15	1.4 (-02)
IRDC015.05-2	0.1 (0.01)	29.5 (0.10)	1.4 (0.25)	7.89(-02)	1.3 (-02)
IRDC015.05-3	0.2 (0.03)	24.3 (0.21)	2.2 (0.49)	8.62(-02)	2.5 (-02)
IRDC018.48-7	6.9(-02)(0.01)	46.4 (0.07)	0.8 (0.16)	7.50(-02)	1.3 (-02)
IRDC018.48-8	5.4(-02)(0.01)	45.0 (0.08)	0.7 (0.16)	6.50(-02)	1.2 (-02)
IRDC019.30-1	0.5 (0.04)	26.0 (0.10)	3.4 (0.33)	0.15	1.7 (-02)
IRDC028.34-3	0.4 (0.04)	78.8 (0.10)	2.1 (0.24)	0.19	1.8 (-02)
IRDC028.34-4	0.1 (0.02)	79.3 (0.25)	2.5 (0.90)	4.38(-02)	1.4 (-02)
IRDC028.34-6	1.3 (0.10)	77.8 (0.10)	3.0 (0.35)	0.40	1.5 (-02)
IRDC048.66-1	0.1 (0.01)	34.0 (0.09)	1.0 (0.22)	9.28(-02)	2.2 (-02)
IRDC048.66-3					1.5 (-02)
IRDC079.31-2	8.7(-02)(0.02)	1.7 (0.17)	1.6 (0.51)	4.90(-02)	1.3 (-02)
ISOSSJ23053	0.3 (0.03)	-52.1 (0.08)	1.8 (0.18)	0.19	1.2 (-02)
CH ₃ CCH 9 ₀ -8 ₀					
IRDC010.70-2	0.2 (0.05)	28.9 (0.13)	1.5 (0.38)	0.15	3.7 (-02)
IRDC010.70-4	0.2 (0.04)	29.1 (0.10)	1.3 (0.27)	0.20	3.9 (-02)
IRDC011.11-2	0.1 (0.02)	30.5 (0.14)	1.6 (0.30)	8.15(-02)	1.9 (-02)
IRDC011.11-4	1.0 (0.08)	29.7 (0.10)	2.7 (0.30)	0.35	3.2 (-02)
IRDC011.11-5					1.1 (-02)
IRDC013.90-1	0.3 (0.02)	22.8 (0.06)	1.6 (0.14)	0.17	1.4 (-02)
IRDC015.05-2	0.1 (0.01)	29.6 (0.09)	1.7 (0.22)	8.81(-02)	1.3 (-02)
IRDC015.05-3	0.2 (0.03)	24.3 (0.11)	1.6 (0.33)	0.13	2.5 (-02)
IRDC018.48-7	0.1 (0.01)	46.5 (0.07)	1.1 (0.15)	8.63(-02)	1.3 (-02)
IRDC018.48-8	9.5(-02)(0.01)	45.0 (0.09)	1.2 (0.18)	6.91(-02)	1.2 (-02)
IRDC019.30-1	0.7 (0.07)	26.2 (0.12)	3.4 (0.60)	0.19	1.7 (-02)
IRDC028.34-3	0.5 (0.03)	78.9 (0.07)	2.0 (0.18)	0.23	1.8 (-02)
IRDC028.34-4	8.3(-02)(0.01)	78.8 (0.10)	1.1 (0.24)	7.00(-02)	1.4 (-02)
IRDC028.34-6	1.5 (0.09)	78.0 (0.08)	3.0 (0.24)	0.47	1.5 (-02)
IRDC048.66-1	9.7(-02)(0.02)	34.1 (0.08)	0.8 (0.23)	0.10	2.2 (-02)
IRDC048.66-3					1.5 (-02)
IRDC079.31-2	0.1 (0.01)	1.7 (0.07)	1.2 (0.14)	9.48(-02)	1.3 (-02)
ISOSSJ23053	0.4 (0.03)	-51.8 (0.05)	1.8 (0.15)	0.24	1.2 (-02)
HNC0 7 _{0,7} -6 _{0,6}					
IRDC010.70-2	0.4 (0.05)	28.9 (0.11)	2.0 (0.33)	0.21	3.7 (-02)

Table 9—Continued

Name	$\int T_A dv$ (K km/s)	V_{lsr} km/s	ΔV km/s	T_A K	1σ rms K
IRDC010.70-4	0.2 (0.05)	29.4 (0.12)	1.5 (0.37)	0.17	3.8 (-02)
IRDC011.11-2	0.1 (0.02)	30.7 (0.10)	1.2 (0.23)	9.55(-02)	2.0 (-02)
IRDC011.11-4	0.6 (0.06)	29.9 (0.11)	2.8 (0.33)	0.23	3.5 (-02)
IRDC011.11-5	8.2(-02)(0.01)	29.6 (0.16)	1.5 (0.41)	5.12(-02)	1.1 (-02)
IRDC013.90-1	0.1 (0.01)	22.8 (0.09)	1.8 (0.21)	8.58(-02)	1.4 (-02)
IRDC015.05-2	0.1 (0.01)	29.5 (0.08)	1.5 (0.21)	8.55(-02)	1.3 (-02)
IRDC015.05-3	0.3 (0.05)	24.1 (0.15)	2.9 (0.63)	0.12	2.4 (-02)
IRDC018.48-7	6.0(-02)(0.01)	46.5 (0.06)	0.7 (0.15)	7.37(-02)	1.2 (-02)
IRDC018.48-8	6.6(-02)(0.01)	44.8 (0.16)	1.4 (0.44)	4.28(-02)	1.2 (-02)
IRDC019.30-1	1.0 (0.04)	26.4 (0.07)	4.7 (0.24)	0.21	1.7 (-02)
IRDC028.34-3	0.3 (0.04)	78.7 (0.21)	4.1 (0.65)	8.01(-02)	1.8 (-02)
IRDC028.34-4	0.2 (0.01)	79.6 (0.09)	2.4 (0.21)	9.85(-02)	1.3 (-02)
IRDC028.34-6	2.7 (0.03)	78.1 (0.02)	3.7 (0.06)	0.68	1.4 (-02)
IRDC048.66-1					2.2 (-02)
IRDC048.66-3	7.8(-02)(0.01)	33.5 (0.12)	1.1 (0.23)	6.37(-02)	1.5 (-02)
IRDC079.31-2	0.1 (0.01)	1.9 (0.04)	1.0 (0.14)	0.12	1.3 (-02)
ISOSSJ23053	0.4 (0.02)	-51.8 (0.05)	2.5 (0.14)	0.16	1.2 (-02)
CH ₃ OH 1 _{1,0} -0 _{0,0} E					
IRDC010.70-2					8.8 (-02)
IRDC010.70-4					8.8 (-02)
IRDC011.11-2					9.3 (-02)
IRDC011.11-4					8.8 (-02)
IRDC011.11-5					8.7 (-02)
IRDC013.90-1					9.0 (-02)
IRDC015.05-2	n/a				
IRDC015.05-3	n/a				
IRDC018.48-7	n/a				
IRDC018.48-8	n/a				
IRDC019.30-1	1.7 (0.16)	26.8 (0.33)	6.7 (0.78)	0.23	8.7 (-02)
IRDC028.34-3	0.6 (0.08)	78.8 (0.16)	2.2 (0.36)	0.25	8.7 (-02)
IRDC028.34-4					8.9 (-02)
IRDC028.34-6	1.8 (0.13)	77.8 (0.14)	3.9 (0.33)	0.43	9.3 (-02)
IRDC048.66-1	n/a				
IRDC048.66-3	n/a				
IRDC079.31-2	n/a				
ISOSSJ23053	n/a				
H ₂ CO 3 _{0,3} -2 _{0,2}					
IRDC010.70-2	1.8 (0.06)	29.1 (0.05)	3.4 (0.16)	0.50	4.9 (-02)
IRDC010.70-4	0.9 (0.06)	29.2 (0.10)	3.3 (0.26)	0.27	5.2 (-02)
IRDC011.11-2	0.4 (0.05)	30.8 (0.19)	2.5 (0.40)	0.15	5.2 (-02)
IRDC011.11-4	1.9 (0.08)	29.7 (0.07)	4.2 (0.23)	0.44	5.0 (-02)
IRDC011.11-5	0.1 (0.03)	29.3 (0.07)	0.6 (0.23)	0.20	3.5 (-02)
IRDC013.90-1	1.2 (0.05)	22.8 (0.03)	1.8 (0.10)	0.64	5.3 (-02)
IRDC015.05-2	0.3 (0.04)	29.5 (0.08)	1.4 (0.17)	0.23	5.0 (-02)
IRDC015.05-3	1.0 (0.08)	24.1 (0.18)	4.9 (0.47)	0.19	5.1 (-02)

Table 9—Continued

Name	$\int T_A dv$ (K km/s)	V_{lsr} km/s	ΔV km/s	T_A K	1σ rms K
IRDC018.48-7	0.1 (0.03)	46.6 (0.14)	1.1 (0.31)	0.12	5.3 (-02)
IRDC018.48-8	0.3 (0.05)	45.7 (0.18)	2.1 (0.32)	0.16	5.6 (-02)
IRDC019.30-1	4.0 (0.08)	26.6 (0.03)	3.9 (0.10)	0.95	5.3 (-02)
IRDC028.34-3	3.5 (0.04)	78.8 (0.02)	3.9 (0.06)	0.85	3.4 (-02)
IRDC028.34-4	0.6 (0.04)	79.2 (0.08)	2.7 (0.23)	0.22	3.6 (-02)
IRDC028.34-6	7.1 (0.06)	78.1 (0.03)	6.7 (0.07)	0.99	3.8 (-02)
IRDC048.66-1	0.5 (0.04)	33.8 (0.06)	1.6 (0.15)	0.30	4.7 (-02)
IRDC048.66-3	0.4 (0.04)	33.4 (0.07)	1.6 (0.23)	0.25	4.4 (-02)
IRDC079.31-2	1.0 (0.02)	1.9 (0.02)	1.5 (0.05)	0.62	3.1 (-02)
ISOSSJ23053	n/a				
H ₂ CO 3 _{2,2} -2 _{2,1}					
IRDC010.70-2	0.4 (0.05)	78.1 (0.18)	2.9 (0.34)	0.15	4.8 (-02)
IRDC010.70-4					5.2 (-02)
IRDC011.11-2					5.2 (-02)
IRDC011.11-4	0.4 (0.07)	30.0 (0.44)	5.0 (1.05)	7.81(-02)	4.5 (-02)
IRDC011.11-5					3.5 (-02)
IRDC013.90-1					4.5 (-02)
IRDC015.05-2					4.5 (-02)
IRDC015.05-3					4.7 (-02)
IRDC018.48-7					4.5 (-02)
IRDC018.48-8					5.1 (-02)
IRDC019.30-1	1.0 (0.14)	26.6 (0.28)	4.6 (0.94)	0.20	4.9 (-02)
IRDC028.34-3	0.6 (0.04)	78.7 (0.09)	3.2 (0.24)	0.18	3.1 (-02)
IRDC028.34-4	0.1 (0.03)	79.4 (0.29)	2.1 (0.53)	5.10(-02)	3.2 (-02)
IRDC028.34-6	2.6 (0.04)	78.2 (0.04)	4.5 (0.09)	0.53	3.1 (-02)
IRDC048.66-1					4.7 (-02)
IRDC048.66-3					2.8 (-02)
IRDC079.31-2	0.1 (0.03)	1.5 (0.31)	2.7 (0.96)	5.25(-02)	2.8 (-02)
ISOSSJ23053	n/a				
H ₂ CO 3 _{2,1} -2 _{2,0}					
IRDC010.70-2					4.8 (-02)
IRDC010.70-4					5.2 (-02)
IRDC011.11-2					5.2 (-02)
IRDC011.11-4	0.5 (0.07)	29.722 (0.32)	4.657 (0.79)	0.1	4.6 (-02)
IRDC011.11-5					3.5 (-02)
IRDC013.90-1					4.5 (-02)
IRDC015.05-2					4.5 (-02)
IRDC015.05-3					4.7 (-02)
IRDC018.48-7					4.5 (-02)
IRDC018.48-8					5.1 (-02)
IRDC019.30-1	1.1 (0.07)	26.519 (0.12)	4.309 (0.42)	0.24	4.6 (-02)
IRDC028.34-3	0.8 (0.05)	78.691 (0.12)	4.501 (0.40)	0.18	3.1 (-02)
IRDC028.34-4					3.2 (-02)
IRDC028.34-6	2.7 (0.05)	78.157 (0.04)	4.851 (0.11)	0.53	3.1 (-02)
IRDC048.66-1					4.7 (-02)

Table 9—Continued

Name	$\int T_A dv$ (K km/s)	V_{lsr} km/s	ΔV km/s	T_A K	1σ rms K
IRDC048.66-3					2.8 (-02)
IRDC079.31-2					2.8 (-02)
ISOSSJ23053	n/a				
CH ₃ OH 4 _{2,2} -3 _{1,2} E					
IRDC010.70-2	0.4 (0.05)	29.2 (0.18)	2.9 (0.345)	0.15	4.8 (-02)
IRDC010.70-4					4.6 (-02)
IRDC011.11-2					4.6 (-02)
IRDC011.11-4	0.4 (0.06)	29.5 (0.16)	3.0 (0.560)	0.15	4.5 (-02)
IRDC011.11-5					3.2 (-02)
IRDC013.90-1					4.5 (-02)
IRDC015.05-2					4.6 (-02)
IRDC015.05-3	0.2 (0.05)	23.5 (0.27)	2.6 (0.464)	0.10	4.7 (-02)
IRDC018.48-7					4.6 (-02)
IRDC018.48-8					5.0 (-02)
IRDC019.30-1	2.0 (0.10)	26.6 (0.09)	4.5 (0.300)	0.42	4.9 (-02)
IRDC028.34-3	1.0 (0.04)	78.8 (0.05)	2.7 (0.164)	0.37	3.2 (-02)
IRDC028.34-4					3.3 (-02)
IRDC028.34-6	5.0 (0.13)	78.1 (0.04)	4.0 (0.126)	1.18	3.1 (-02)
IRDC048.66-1					4.1 (-02)
IRDC048.66-3					2.8 (-02)
IRDC079.31-2					2.8 (-02)
ISOSSJ23053	n/a				
C ¹⁸ O 2-1					
IRDC010.70-2	5.8 (0.12)	28.6 (0.02)	2.3 (0.06)	2.38	4.3 (-02)
IRDC010.70-4	6.8 (0.05)	29.2 (0.00)	1.7 (0.01)	3.75	4.5 (-02)
IRDC011.11-2	4.6 (0.04)	30.2 (0.01)	2.1 (0.02)	2.02	4.2 (-02)
IRDC011.11-4	4.1 (0.00)	29.5 (0.00)	1.5 (0.01)	2.54	4.1 (-02)
IRDC011.11-5	3.8 (0.04)	29.6 (0.01)	2.1 (0.03)	1.71	3.0 (-02)
IRDC013.90-1	9.6 (0.08)	23.1 (0.01)	3.1 (0.03)	2.91	4.7 (-02)
IRDC015.05-2	4.1 (0.07)	29.6 (0.01)	1.6 (0.03)	2.29	4.6 (-02)
IRDC015.05-3	7.2 (0.05)	24.3 (0.01)	2.5 (0.02)	2.72	5.4 (-02)
IRDC018.48-7	3.7 (0.12)	46.4 (0.02)	1.3 (0.05)	2.51	4.5 (-02)
IRDC018.48-8	4.1 (0.08)	45.0 (0.01)	1.4 (0.04)	2.64	4.6 (-02)
IRDC019.30-1	5.9 (0.05)	26.3 (0.01)	2.5 (0.02)	2.14	4.7 (-02)
IRDC028.34-3	8.1 (0.04)	78.2 (0.01)	5.5 (0.03)	1.38	2.9 (-02)
IRDC028.34-4	6.3 (0.05)	79.2 (0.01)	3.6 (0.03)	1.63	3.3 (-02)
IRDC028.34-6	14. (0.08)	78.0 (0.00)	2.9 (0.02)	4.53	3.1 (-02)
IRDC048.66-1	3.5 (0.03)	33.6 (0.00)	1.4 (0.01)	2.31	3.8 (-02)
IRDC048.66-3	2.3 (0.03)	33.4 (0.01)	1.6 (0.02)	1.35	2.6 (-02)
IRDC079.31-2	3.9 (0.09)	1.7 (0.01)	1.2 (0.03)	2.90	2.4 (-02)
ISOSSJ23053	n/a				

Note. — Blank spaces indicate non-detections and n/a indicates absence of data

Table 10: Observational and modeled abundances for IRDC028.34-6 with respect to H₂.

Species	Observations	Model (time= 3×10^5 yr ^a)					
		T=30 K ^b n= 10^5 cm ⁻³ t _{cold} = 10^6 yr T \propto time ² 1% ^c	T=30 K ^b n= 10^5 cm ⁻³ t _{cold} = 10^6 yr T \propto time ² 10%	T=30 K n=10^6 cm⁻³ t _{cold} = 10^6 yr T \propto time ² 1%	T=30 K n= 10^5 cm ⁻³ t _{cold} = 10^5 yr T \propto time ² 1%	T=40 K n= 10^5 cm ⁻³ t _{cold} = 10^6 yr T \propto time ² 1%	T=30 K n= 10^5 cm ⁻³ t _{cold} = 10^6 yr T\proptotime 1%
CO	2.1(-04)	4.4(-05)	5.0(-05)	5.8(-05)	7.6(-05)	7.0(-05)	4.8(-05)
H ₂ CO	3.1(-09)	2.2(-08)	7.7(-08)	2.8(-09)	6.0(-09)	6.6(-08)	1.4(-08)
CH ₃ OH	4.0(-08)	2.6(-11)	2.2(-10)	5.4(-11)	1.5(-12)	1.0(-10)	2.3(-11)
HNCO	5.8(-10)	2.0(-10)	1.5(-09)	3.7(-11)	7.0(-10)	1.1(-11)	2.0(-10)
CH ₃ CCH	3.4(-09)	2.1(-09)	1.1(-08)	8.9(-10)	1.2(-09)	3.4(-09)	1.2(-09)
CH ₃ CHO	1.1(-09)	4.8(-10)	9.6(-09)	8.4(-11)	1.6(-11)	3.2(-10)	3.5(-10)
CH ₃ OCH ₃	<1.9(-09)	1.1(-12)	1.1(-11)	3.5(-12)	2.4(-14)	3.7(-14)	8.3(-13)
CH ₃ OCHO	3.7(-10)	4.4(-11)	4.8(-10)	4.6(-12)	3.7(-14)	6.9(-13)	3.7(-11)
N ₂ H ⁺	1.1(-09) ^d	3.3(-10)	3.5(-10)	2.5(-11)	2.3(-10)	1.8(-10)	3.0(-10)
HCCCN	3.6(-10) ^d	1.4(-09)	5.7(-09)	1.0(-10)	8.3(-11)	1.7(-08)	9.4(-10)
HNC	1.4(-08) ^d	4.2(-09)	1.1(-08)	2.5(-10)	7.5(-10)	5.2(-08)	3.4(-09)
HCO ⁺	6.2(-09) ^d	6.3(-09)	5.7(-09)	2.6(-09)	7.6(-09)	6.2(-09)	6.2(-09)
C ₂ H	1.0(-08) ^d	2.7(-08)	2.6(-08)	1.0(-08)	1.8(-09)	2.3(-08)	1.9(-08)
NH ₃	1.2(-08) ^e	2.3(-08)	2.9(-08)	2.0(-09)	1.5(-08)	1.3(-08)	1.3(-08)

Note: a(b) = $a \times 10^b$. Boldface indicate more than one order of magnitude disagreement between model and observations.

^a Model result at moment of the best fit for the standard model .

^b Maximum temperature of warm-up phase.

^c Reactive desorption efficiency.

^d Data taken from Sanhueza et al. (2012).

^e Data taken from Wienen et al. (2012).

REFERENCES

- Arce, H. G., Santiago-García, J., Jørgensen, J. K., Tafalla, M., & Bachiller, R. 2008, *ApJ*, 681, L21
- Bacmann, A., Taquet, V., Faure, A., Kahane, C., & Ceccarelli, C. 2012, *A&A*, 541, L12
- Belloche, A., Garrod, R. T., Müller, H. S. P., Menten, K. M., Comito, C., & Schilke, P. 2009, *A&A*, 499, 215
- Belloche, A., Menten, K. M., Comito, C., Müller, H. S. P., Schilke, P., Ott, J., Thorwirth, S., & Hieret, C. 2008, *A&A*, 482, 179
- Beuther, H., Churchwell, E. B., McKee, C. F., & Tan, J. C. 2007, *Protostars and Planets V*, 165
- Beuther, H. & Sridharan, T. K. 2007, *ApJ*, 668, 348
- Birkmann, S. M., Krause, O., Hennemann, M., Henning, T., Steinacker, J., & Lemke, D. 2007, *A&A*, 474, 883
- Bottinelli, S., Ceccarelli, C., Lefloch, B., Williams, J. P., Castets, A., Caux, E., Cazaux, S., Maret, S., Parise, B., & Tielens, A. G. G. M. 2004, *ApJ*, 615, 354
- Butler, M. J. & Tan, J. C. 2009, *ApJ*, 696, 484
- Carey, S. J., Clark, F. O., Egan, M. P., Price, S. D., Shipman, R. F., & Kuchar, T. A. 1998, *ApJ*, 508, 721
- Carey, S. J., Feldman, P. A., Redman, R. O., Egan, M. P., MacLeod, J. M., & Price, S. D. 2000, *ApJ*, 543, L157
- Cernicharo, J., Marcelino, N., Roueff, E., Gerin, M., Jiménez-Escobar, A., & Muñoz Caro, G. M. 2012, *ApJ*, 759, L43

- Chambers, E. T., Jackson, J. M., Rathborne, J. M., & Simon, R. 2009, *ApJS*, 181, 360
- Charnley, S. B., Tielens, A. G. G. M., & Rodgers, S. D. 1997, *ApJ*, 482, L203
- Cyganowski, C. J., Whitney, B. A., Holden, E., Braden, E., Brogan, C. L., Churchwell, E.,
Indebetouw, R., Watson, D. F., Babler, B. L., Benjamin, R., Gomez, M., Meade,
M. R., Povich, M. S., Robitaille, T. P., & Watson, C. 2008, *AJ*, 136, 2391
- Egan, M. P., Shipman, R. F., Price, S. D., Carey, S. J., Clark, F. O., & Cohen, M. 1998,
ApJ, 494, L199+
- Garrod, R. T. & Herbst, E. 2006, *A&A*, 457, 927
- Garrod, R. T., Wakelam, V., & Herbst, E. 2007, *A&A*, 467, 1103
- Garrod, R. T., Weaver, S. L. W., & Herbst, E. 2008, *ApJ*, 682, 283
- Gibson, D., Plume, R., Bergin, E., Ragan, S., & Evans, N. 2009, *ApJ*, 705, 123
- Goldsmith, P. F. & Langer, W. D. 1999, *ApJ*, 517, 209
- Graedel, T. E., Langer, W. D., & Frerking, M. A. 1982, *ApJS*, 48, 321
- He, J. H., Takahashi, S., & Chen, X. 2012, *ApJS*, 202, 1
- Helmich, F. P. & van Dishoeck, E. F. 1997, *A&AS*, 124, 205
- Hernandez, A. K., Tan, J. C., Caselli, P., Butler, M. J., Jiménez-Serra, I., Fontani, F., &
Barnes, P. 2011, *ApJ*, 738, 11
- Hoq, S., Jackson, J. M., Foster, J. B., Sanhueza, P., Guzman, A., Whitaker, J. S.,
Clayton, C., Rathborne, J. M., Vasyunina, T., & Vasyunin, A. 2013, *ArXiv*
e-prints

- Horn, A., Møllendal, H., Sekiguchi, O., Uggerud, E., Roberts, H., Herbst, E., Viggiano, A. A., & Fridgen, T. D. 2004, *ApJ*, 611, 605
- Ikeda, M., Ohishi, M., Nummelin, A., Dickens, J. E., Bergman, P., Hjalmarson, Å., & Irvine, W. M. 2001, *ApJ*, 560, 792
- Kauffmann, J. & Pillai, T. 2010, *ApJ*, 723, L7
- Klein, B., Hochgürtel, S., Krämer, I., Bell, A., Meyer, K., & Güsten, R. 2012, *A&A*, 542, L3
- Ladd, N., Purcell, C., Wong, T., & Robertson, S. 2005, *Publications of the Astronomical Society of Australia*, 22, 62
- Lee, M., Stanimirović, S., Ott, J., van Loon, J. T., Bolatto, A. D., Jones, P. A., Cunningham, M. R., Devine, K. E., & Oliveira, J. M. 2009, *AJ*, 138, 1101
- Leurini, S., Schilke, P., Wyrowski, F., & Menten, K. M. 2007, *A&A*, 466, 215
- Marcelino, N., Cernicharo, J., Tercero, B., & Roueff, E. 2009, *ApJ*, 690, L27
- Miettinen, O. 2012, *A&A*, 540, A104
- Morton, D. C. 1974, *ApJ*, 193, L35
- Müller, H. S. P., Schlöder, F., Stutzki, J., & Winnewisser, G. 2005, *Journal of Molecular Structure*, 742, 215
- Müller, H. S. P., Thorwirth, S., Roth, D. A., & Winnewisser, G. 2001, *A&A*, 370, L49
- Mundy, L. G., Evans, II, N. J., Snell, R. L., & Goldsmith, P. F. 1987, *ApJ*, 318, 392
- Öberg, K. I., Fuchs, G. W., Awad, Z., Fraser, H. J., Schlemmer, S., van Dishoeck, E. F., & Linnartz, H. 2007, *ApJ*, 662, L23

- Ohishi, M., Irvine, W. M., & Kaifu, N. 1992, in IAU Symposium, Vol. 150, Astrochemistry of Cosmic Phenomena, ed. P. D. Singh, 171–+
- Ossenkopf, V. & Henning, T. 1994, *A&A*, 291, 943
- Perault, M., Omont, A., Simon, G., Seguin, P., Ojha, D., Blommaert, J., Felli, M., Gilmore, G., Guglielmo, F., Habing, H., Price, S., Robin, A., de Batz, B., Cesarsky, C., Elbaz, D., Epchtein, N., Fouque, P., Guest, S., Levine, D., Pollock, A., Prusti, T., Siebenmorgen, R., Testi, L., & Tiphene, D. 1996, *A&A*, 315, L165
- Peretto, N. & Fuller, G. A. 2009, *A&A*, 505, 405
- Pickett, H. M., Poynter, R. L., Cohen, E. A., Delitsky, M. L., Pearson, J. C., & Müller, H. S. P. 1998, *J. Quant. Spec. Radiat. Transf.*, 60, 883
- Pillai, T., Wyrowski, F., Carey, S. J., & Menten, K. M. 2006, *A&A*, 450, 569
- Pitann, J., Linz, H., Ragan, S., Stutz, A. M., Beuther, H., Henning, T., Krause, O., Launhardt, R., Schmiedeke, A., Schuller, F., Tackenberg, J., & Vasyunina, T. 2013, *ApJ*, 766, 68
- Ragan, S., Henning, T., Krause, O., Pitann, J., Beuther, H., Linz, H., Tackenberg, J., Balog, Z., Hennemann, M., Launhardt, R., Lippok, N., Nielbock, M., Schmiedeke, A., Schuller, F., Steinacker, J., Stutz, A., & Vasyunina, T. 2012, *A&A*, 547, A49
- Ragan, S. E., Bergin, E. A., Plume, R., Gibson, D. L., Wilner, D. J., O’Brien, S., & Hails, E. 2006, *ApJS*, 166, 567
- Ragan, S. E., Bergin, E. A., & Wilner, D. 2011, *ApJ*, 736, 163
- Rathborne, J. M., Garay, G., Jackson, J. M., Longmore, S., Zhang, Q., & Simon, R. 2011, *ApJ*, 741, 120

- Rathborne, J. M., Jackson, J. M., Chambers, E. T., Stojimirovic, I., Simon, R., Shipman, R., & Frieswijk, W. 2010, *ApJ*, 715, 310
- Rathborne, J. M., Jackson, J. M., & Simon, R. 2006, *ApJ*, 641, 389
- Rathborne, J. M., Jackson, J. M., Zhang, Q., & Simon, R. 2008, *ApJ*, 689, 1141
- Remijan, A., Snyder, L. E., Friedel, D. N., Liu, S.-Y., & Shah, R. Y. 2003, *ApJ*, 590, 314
- Remijan, A., Snyder, L. E., Liu, S.-Y., Mehringer, D., & Kuan, Y.-J. 2002, *ApJ*, 576, 264
- Requena-Torres, M. A., Martín-Pintado, J., Rodríguez-Franco, A., Martín, S., Rodríguez-Fernández, N. J., & de Vicente, P. 2006, *A&A*, 455, 971
- Ryter, C. E. 1996, *Ap&SS*, 236, 285
- Saito, H., Mizuno, N., Moriguchi, Y., Matsunaga, K., Onishi, T., Mizuno, A., & Fukui, Y. 2001, *PASJ*, 53, 1037
- Sakai, T., Sakai, N., Furuya, K., Aikawa, Y., Hirota, T., & Yamamoto, S. 2012, *ApJ*, 747, 140
- Sakai, T., Sakai, N., Hirota, T., & Yamamoto, S. 2010, *ApJ*, 714, 1658
- Sakai, T., Sakai, N., Kamegai, K., Hirota, T., Yamaguchi, N., Shiba, S., & Yamamoto, S. 2008, *ApJ*, 678, 1049
- Sanhueza, P., Jackson, J. M., Foster, J. B., Garay, G., Silva, A., & Finn, S. C. 2012, *ApJ*, 756, 60
- Schuller, F., Menten, K. M., Contreras, Y., Wyrowski, F., Schilke, P., Bronfman, L., Henning, T., Walmsley, C. M., Beuther, H., Bontemps, S., Cesaroni, R., Deharveng, L., Garay, G., Herpin, F., Lefloch, B., Linz, H., Mardones, D., Minier, V., Molinari,

- S., Motte, F., Nyman, L.-Å., Reveret, V., Risacher, C., Russeil, D., Schneider, N., Testi, L., Troost, T., Vasyunina, T., Wienen, M., Zavagno, A., Kovacs, A., Kreysa, E., Siringo, G., & Weiß, A. 2009, *A&A*, 504, 415
- Semenov, D., Hersant, F., Wakelam, V., Dutrey, A., Chapillon, E., Guilloteau, S., Henning, T., Launhardt, R., Piétu, V., & Schreyer, K. 2010, *A&A*, 522, A42
- Simon, R., Jackson, J. M., Rathborne, J. M., & Chambers, E. T. 2006, *ApJ*, 639, 227
- Sridharan, T. K., Beuther, H., Schilke, P., Menten, K. M., & Wyrowski, F. 2002, *ApJ*, 566, 931
- Sutton, E. C., Peng, R., Danchi, W. C., Jaminet, P. A., Sandell, G., & Russell, A. P. G. 1995, *ApJS*, 97, 455
- Tafalla, M., Santiago-García, J., Myers, P. C., Caselli, P., Walmsley, C. M., & Crapsi, A. 2006, *A&A*, 455, 577
- Vassilev, V., Meledin, D., Lapkin, I., Belitsky, V., Nyström, O., Henke, D., Pavolotsky, A., Monje, R., Risacher, C., Olberg, M., Strandberg, M., Sundin, E., Fredrixon, M., Ferm, S.-E., Desmaris, V., Dochev, D., Pantaleev, M., Bergman, P., & Olofsson, H. 2008, *A&A*, 490, 1157
- Vasyunin, A. I. & Herbst, E. 2013a, *ApJ*, 762, 86
- . 2013b, *ApJ*, 769, 34
- Vasyunina, T., Linz, H., Henning, T., Stecklum, B., Klose, S., & Nyman, L.-Å. 2009, *A&A*, 499, 149 (Paper I)
- Vasyunina, T., Linz, H., Henning, T., Zinchenko, I., Beuther, H., & Voronkov, M. 2011, *A&A*, 527, A88+

Vasyunina, T., Vasyunin, A. I., Herbst, E., & Linz, H. 2012, *ApJ*, 751, 105

Viti, S., Codella, C., Benedettini, M., & Bachiller, R. 2004, *MNRAS*, 350, 1029

Wakelam, V. & Herbst, E. 2008, *ApJ*, 680, 371

Watanabe, N. & Kouchi, A. 2002, *ApJ*, 571, L173

Wienen, M., Wyrowski, F., Schuller, F., Menten, K. M., Walmsley, C. M., Bronfman, L., & Motte, F. 2012, *A&A*, 544, A146

Wouterloot, J. G. A., Walmsley, C. M., & Henkel, C. 1988, *A&A*, 203, 367

Zhang, Q., Wang, Y., Pillai, T., & Rathborne, J. 2009, *ApJ*, 696, 268

Zinchenko, I., Henkel, C., & Mao, R. Q. 2000, *A&A*, 361, 1079

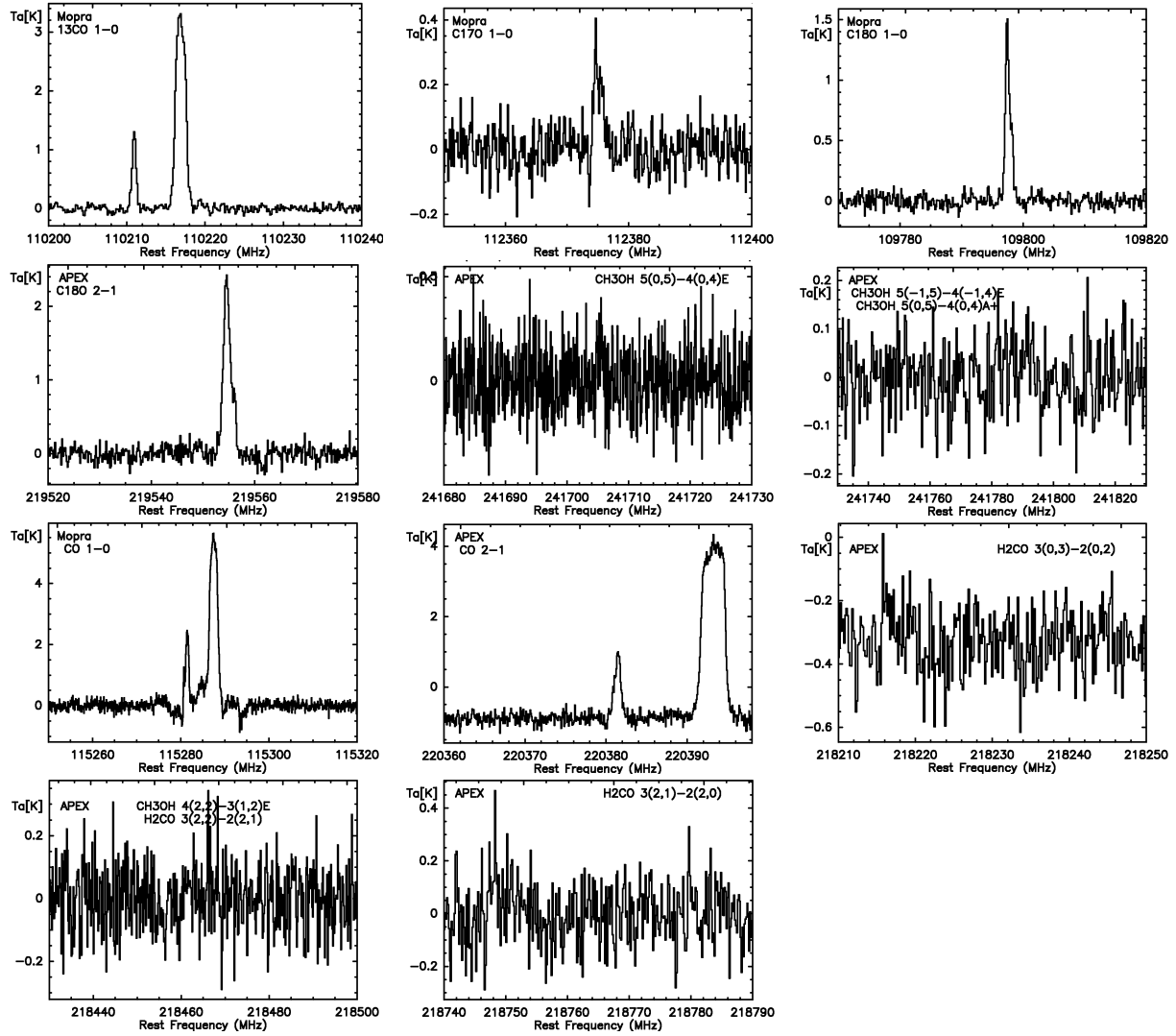


Fig. 1.— Line spectra for IRDC309.37-3.

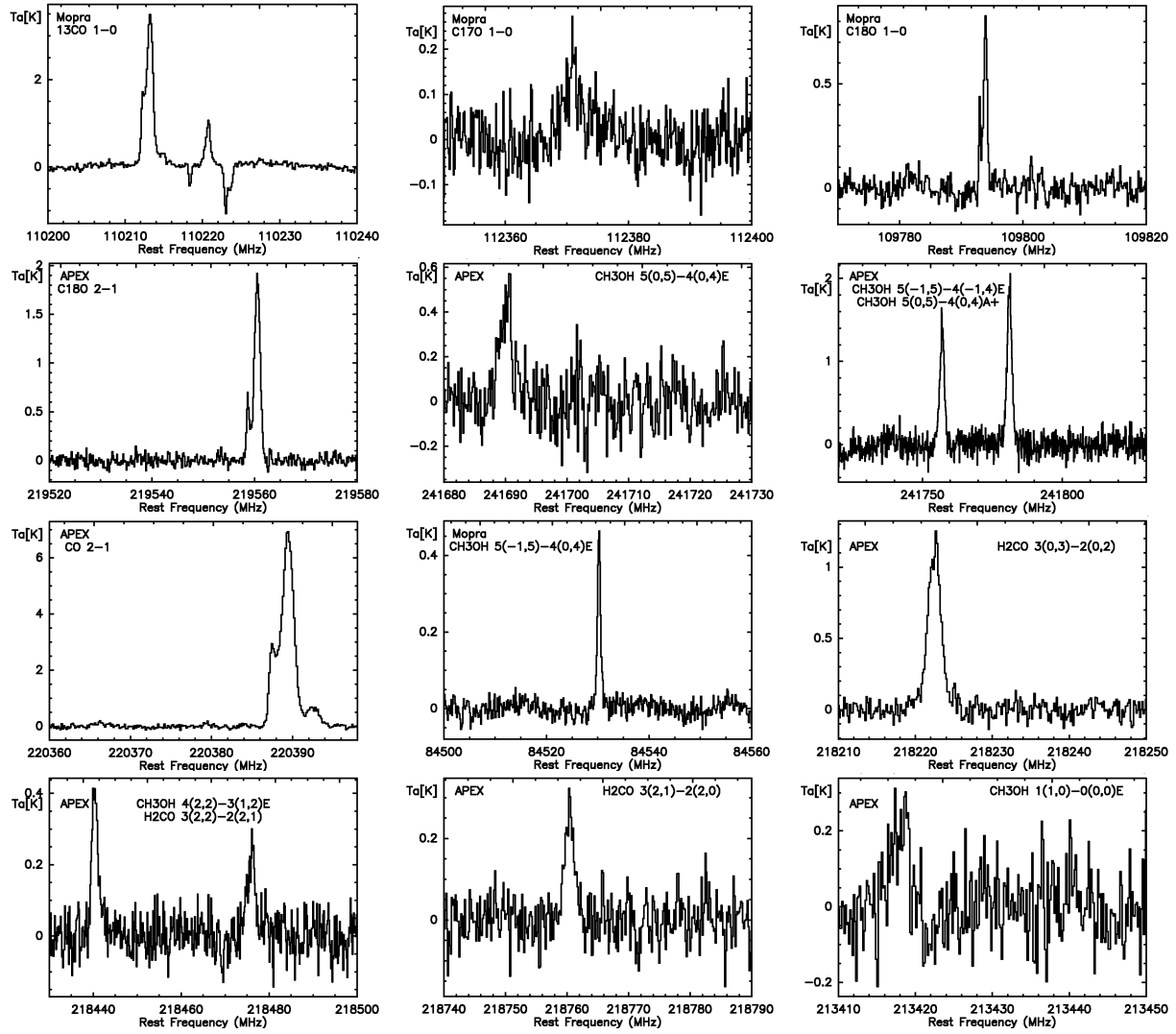


Fig. 2.— Line spectra for IRDC321.73-1.

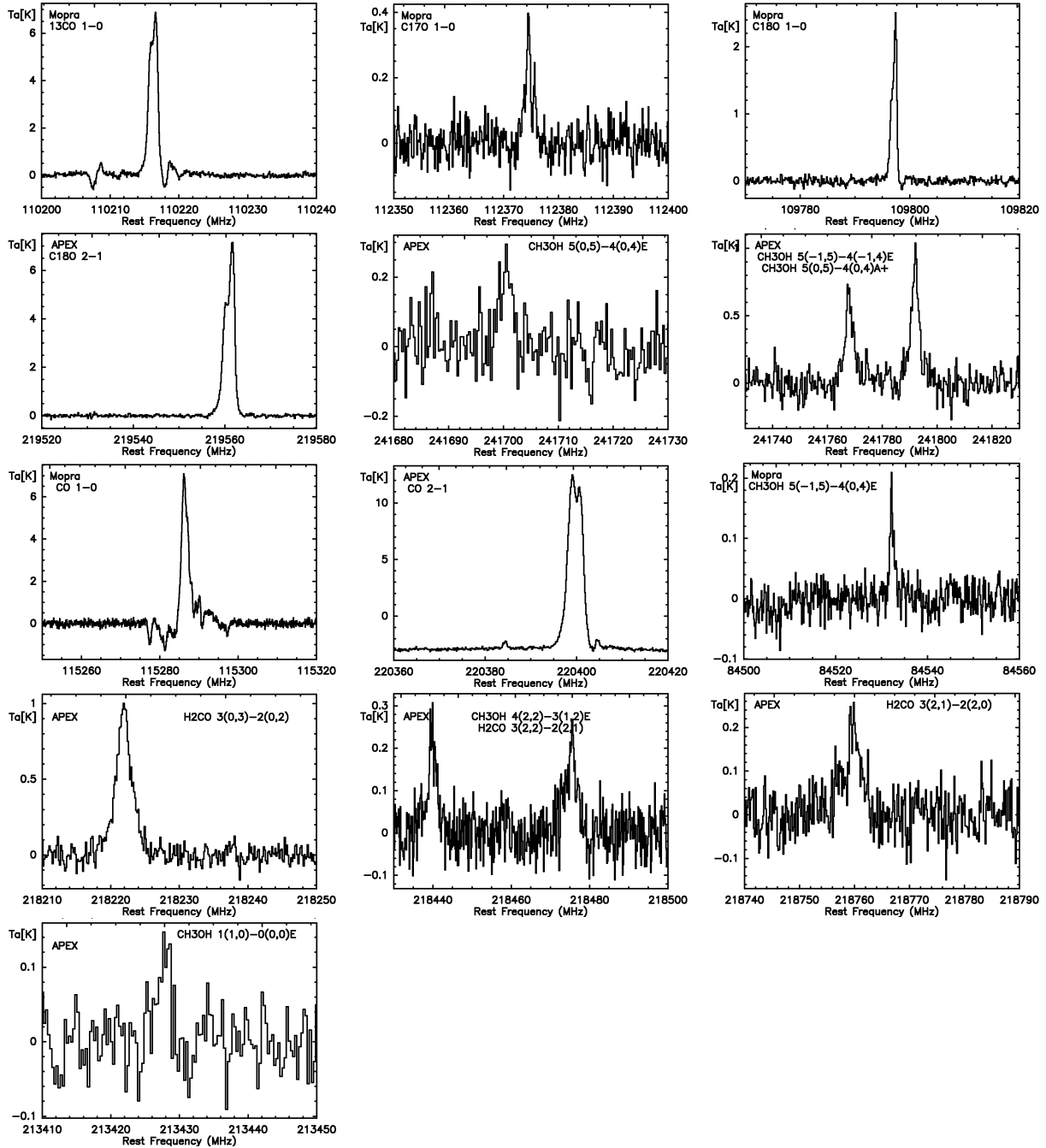


Fig. 3.— Line spectra for IRDC316.76-1.

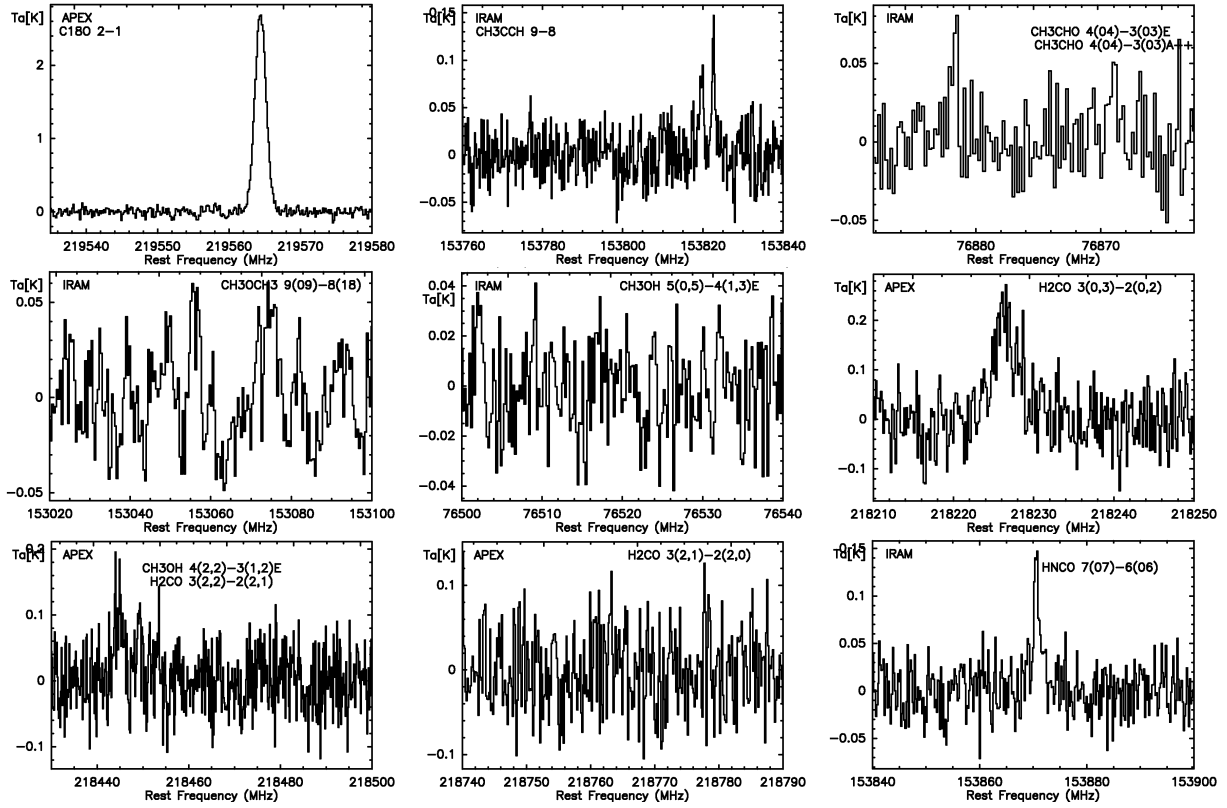


Fig. 4.— Line spectra for IRDC015.05-3.

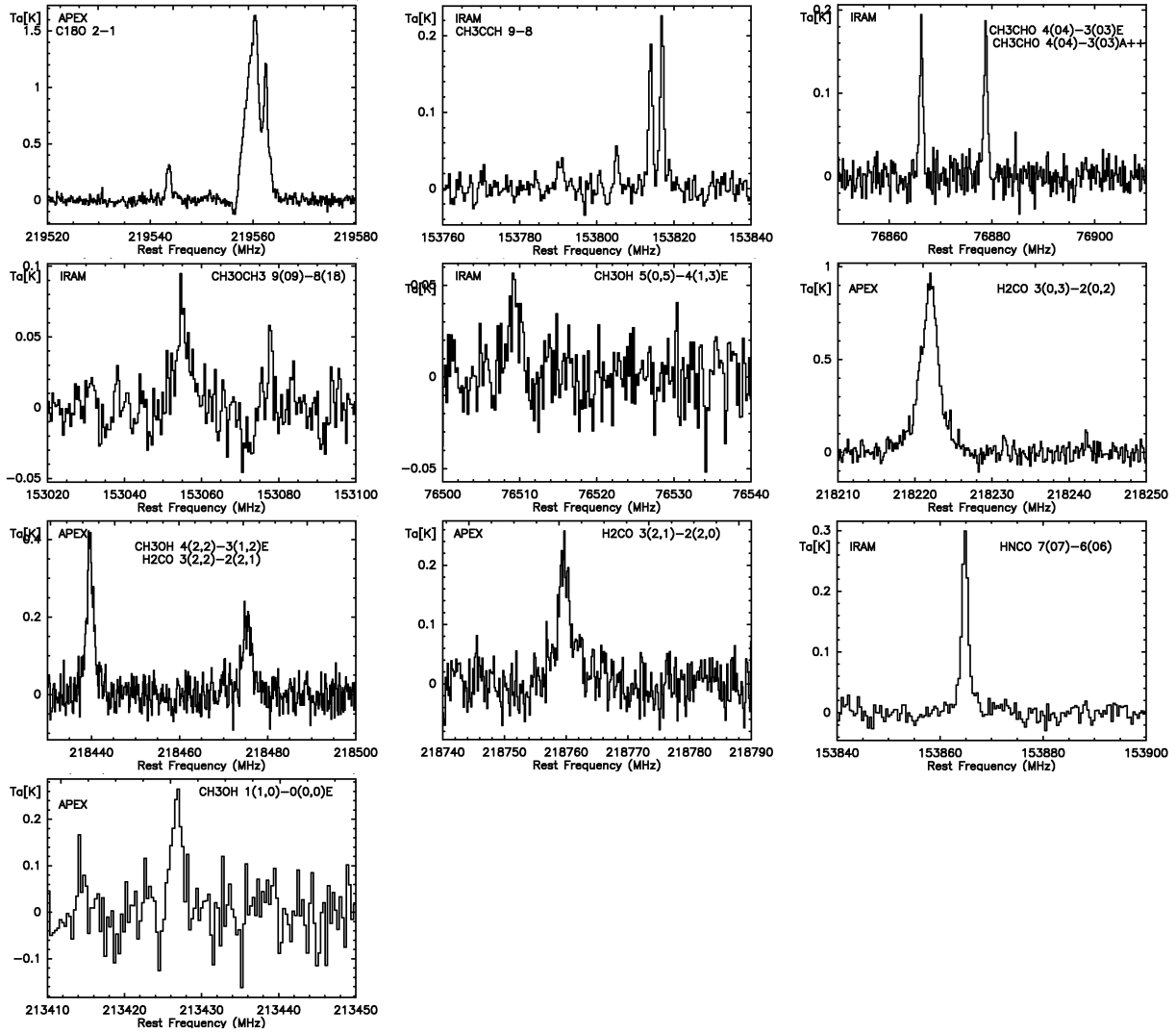


Fig. 5.— Line spectra for IRDC028.34-3.

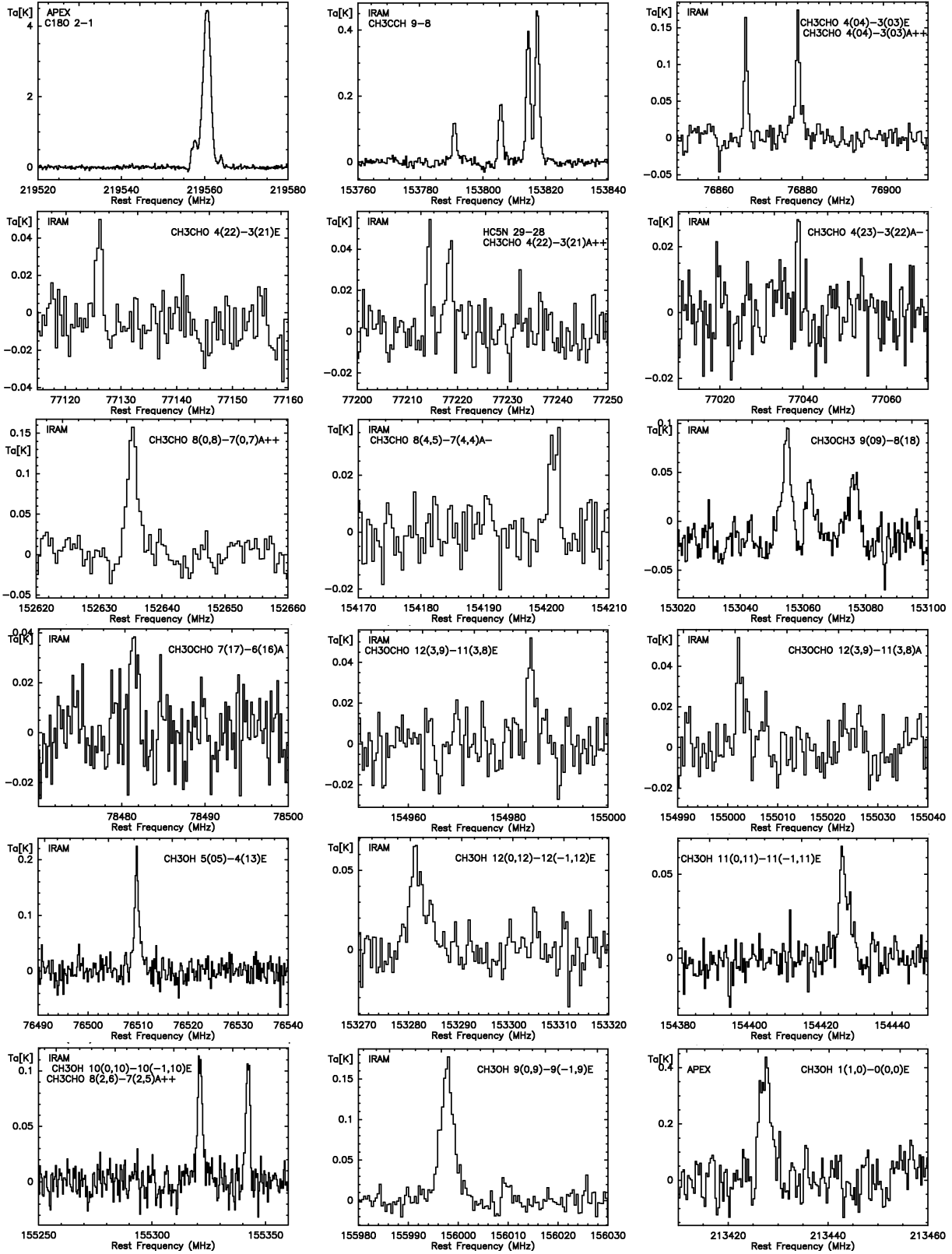


Fig. 6.— Line spectra for IRDC028.34-6.

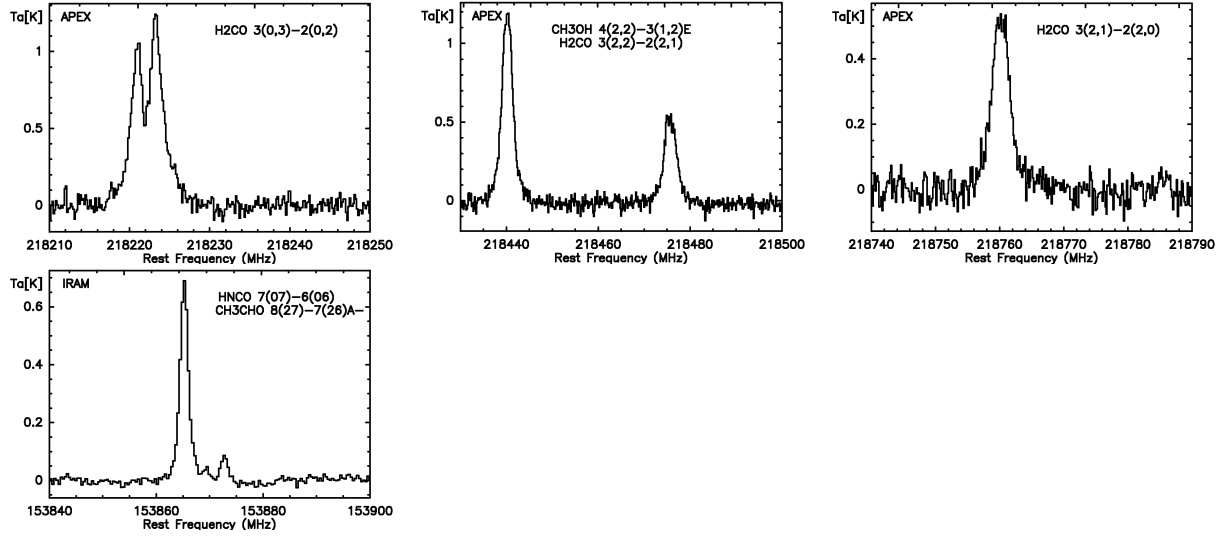


Fig. 7.— Line spectra for IRDC028.34-6 (Continued).

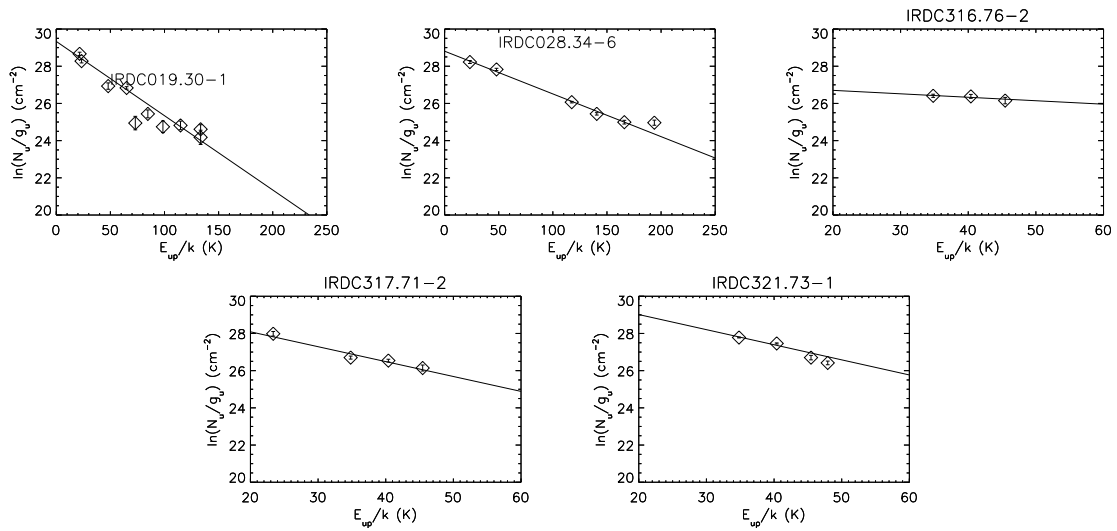


Fig. 8.— Excitation diagrams for CH₃OH.

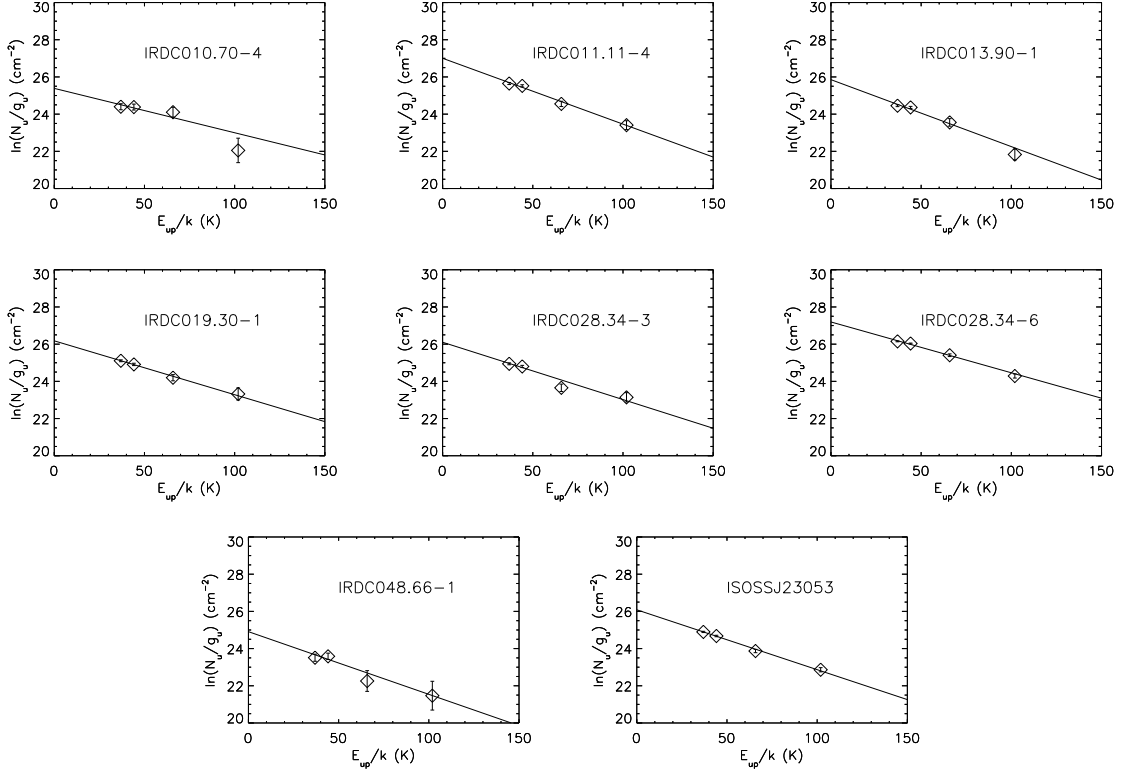


Fig. 9.— Excitation diagrams for CH_3CCH .

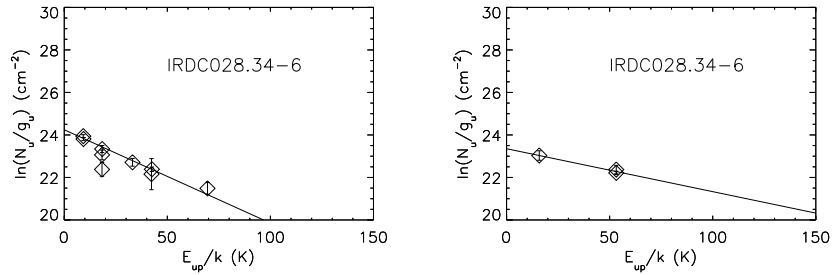


Fig. 10.— Excitation diagrams for CH_3CHO (left) and CH_3OCHO (right).

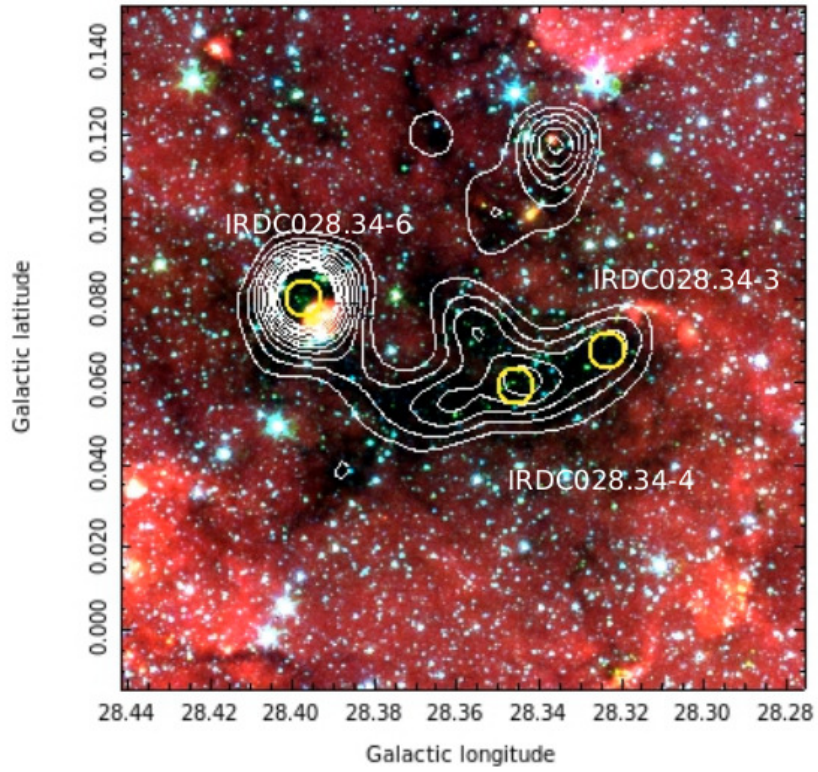


Fig. 11.— Spitzer/GLIMPSE 3-color image of IRDC028.34+0.06, where 3.6 μm is shown in blue, 4.5 μm in green, and 8.0 μm in red. White contours show APEX 870 μm emission. Circles mark observed positions and show the IRAM beam size at 154 GHz.

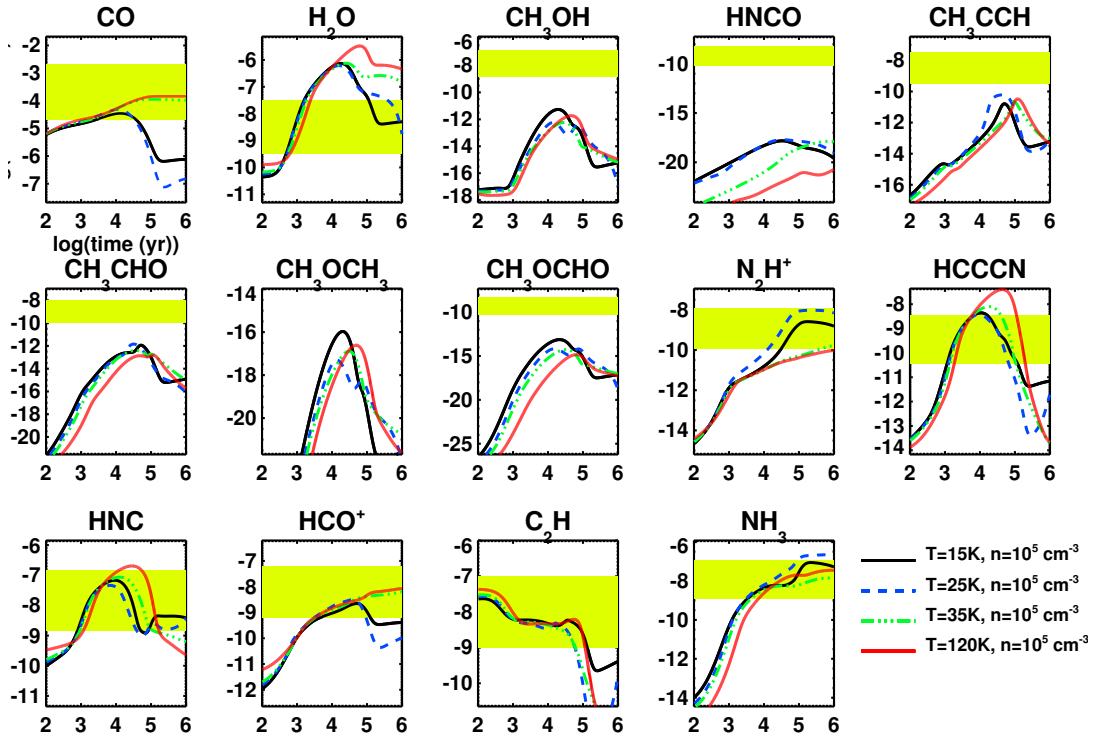


Fig. 12.— Calculated fractional abundances relative to H_2 as a function of time for 14 gas-phase species. Different lines correspond to different temperatures and boxes correspond to the observed values in IRDC028.34-6 \pm one order of magnitude. For these calculations, we used a 0-D pseudo time dependent model.

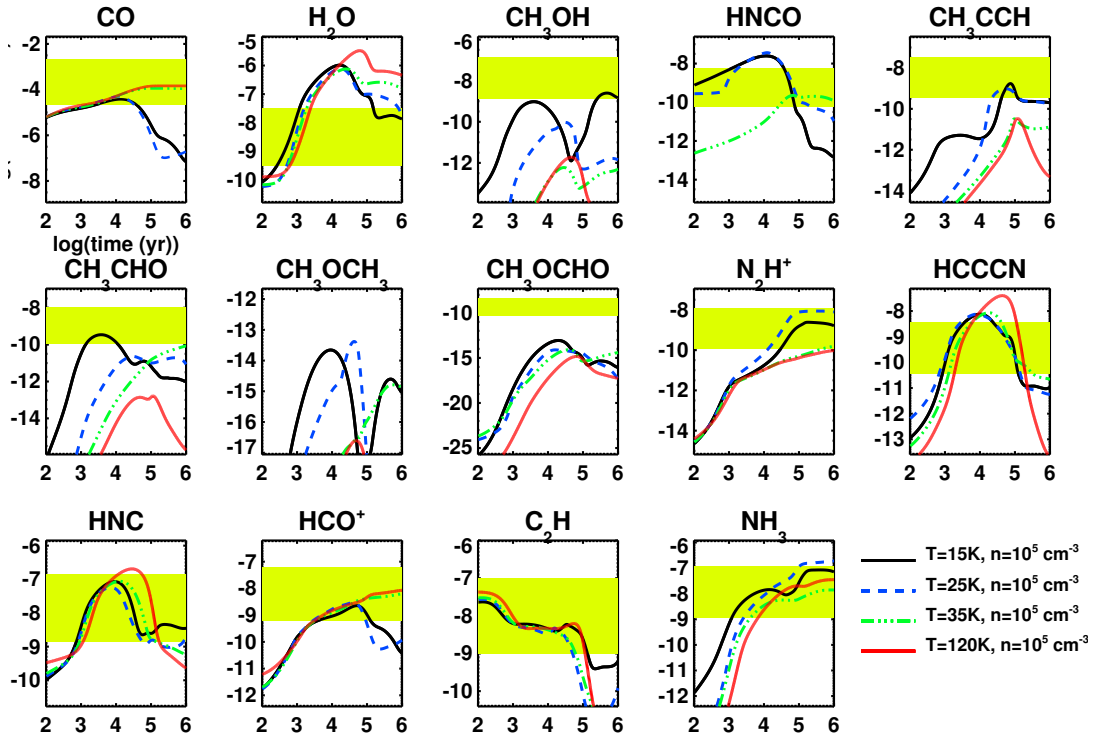


Fig. 13.— Calculated fractional abundances relative to H_2 as a function of time for 14 gas-phase species. Different lines correspond to different temperatures and boxes correspond to the observed values in IRDC028.34-6 \pm one order of magnitude. For these calculations, we used a 0-D pseudo time dependent model including reactive desorption.

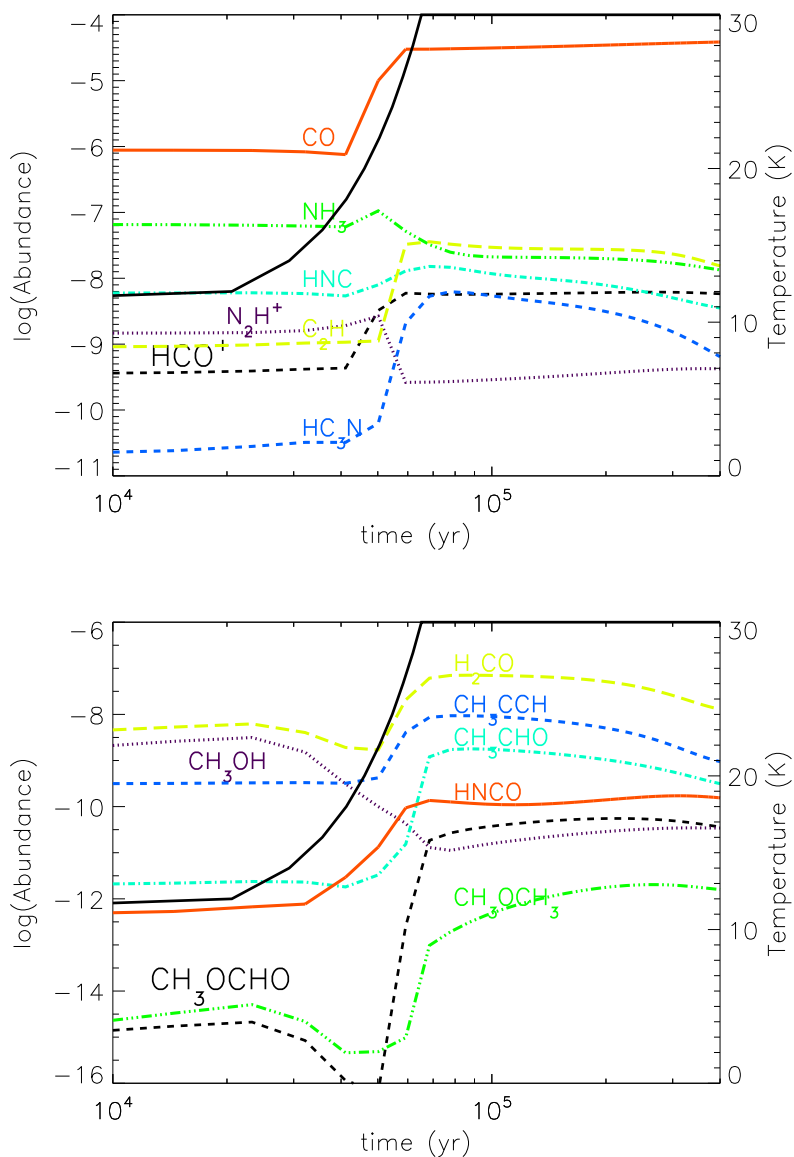


Fig. 14.— Upper panels: Calculated fractional abundances relative to H₂ for our standard warm-up model as a function of time for 14 gas-phase species starting 10^4 yr into the warm-up phase and ending at the 4×10^5 yr. The duration of the 10 K cold phase is 10^6 yr and that of the warm-up phase is 6.5×10^4 yr, with $T \propto \text{time}^2$, a maximum temperature of 30 K, and a constant density of 10^5 cm^{-3} . On all panels, the black solid line indicates the temperature evolution with time.

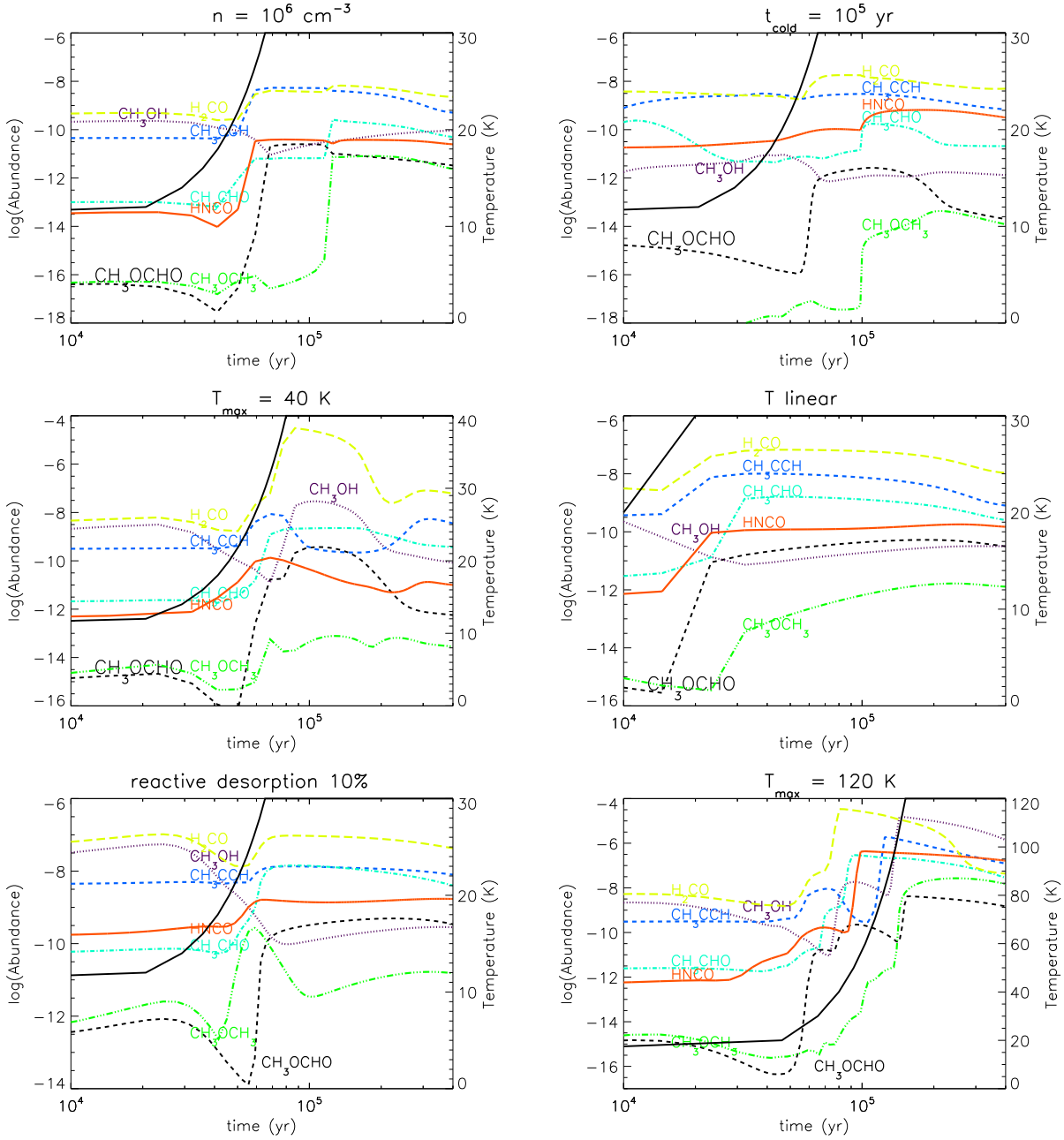


Fig. 15.— Calculated fractional abundances relative to H₂ as a function of time for seven species discussed in the paper. Different panels correspond to models with specific parameters different from those of the standard model. Upper left panel: density $n = 10^6 \text{ cm}^{-3}$; upper right panel: cold phase of 10^5 yr ; middle left panel: maximum temperature of 40 K; middle right panel: linear increase of the temperature from 10 to 30 K. On all panels, the black solid line indicates the temperature evolution with time; lower left panel: reactive desorption efficiency is 10% instead of 1%; lower right panel: maximum temperature of 120 K.